Revision 1

Bubble formation during decompression of andesitic melts

Adrian Fiege[1], François Holtz[1], and Sarah B. Cichy[2]

[1]Institut für Mineralogie, Leibniz Universität Hannover, Callinstraße 3, 30167 Hannover, Germany

[2]Laboratoire Magmas et Volcans, UMR 65, Université Blaise Pascal, 5 rue Kessler, 63038 Clermont-Ferrand Cedex, France

E-mail: **afiege@umich.edu**, f.holtz@mineralogie.uni-hannover.de, s.cichy@opgc.univ-bpclermont.fr

Fax: +49 511 762 3045

Phone: +49 511 762 5281

ABSTRACT

Bubble formation during continuous decompression from ~400 to ~70 MPa was investigated experimentally in hydrous andesitic melts at T = 1030°C and at an oxygen fugacity (fO_2) of about log(fO_2/bar) = QFM+1 (QFM: quartz-fayalite-magnetite buffer). Experiments were carried out at variable decompression rates (r), ranging from 0.0005 to 0.1 MPa/s. The samples were directly quenched after decompression, allowing the investigation of the influence of r on the bubble formation. The effect of variable annealing times (t_A) after decompression was also investigated for experiments performed at a decompression rate of 0.1 MPa/s. These samples were annealed for t_A = 0 to 72 h at final pressure (70 MPa) in order to study changes in

vesiculation during magma storage at shallow depths after fast ascent. Back scattered electron (BSE) images of the samples were analyzed to determine bubble number densities (*BND*).

The *BND* values increase strongly with increasing r and vary from about $10^{2.2}$ mm^{-3} at 0.0005 MPa/s to about $10^{4.6}$ mm^{-3} at 0.1 MPa/s. After fast decompression (r ~ 0.1 MPa/s), the *BND* decrease significantly with t_A, i.e., from ~$10^{4.6}$ mm^{-3} at t_A = 0 h to ~$10^{2.9}$ mm^{-3} at t_A = 72 h. A comparison of the derived *BND* values with recently published experimental data demonstrates the essential role of the decompression path on bubble formation. The *BND* are higher in experiments with multi- or single-step decompression when compared to continuous decompression. The new data show that H_2O-undersaturated andesitic melts are characterized by 1 to 2 log units higher *BND* values than H_2O-saturated rhyolitic melts after decompression with the same rate, indicating a strong influence of melt composition on bubble nucleation. This compositional effect is not predicted accurately by existing models and the interpretation of the vesicularity of dacitic to andesitic melts may lead to overestimations of magma ascent rates by about an order of magnitude.

Keywords: Bubble formation, bubble number density, andesite, continuous decompression

INTRODUCTION

Decompression induced degassing of a magma is a key factor controlling the style of a volcanic eruption (e.g., review of Sparks et al., 1994). Thus, a good knowledge of bubble forming processes in magmatic systems is a pre-requisite to improve our understanding of hazardous, explosive eruptions and pyroclastic flows (see review of Sparks et al. 1994). However, experimental data at geologically relevant conditions in magmatic systems are rare, especially at low, constant decompression rates (r). Continuous decompression experiments, aiming to

understand the formation of bubbles in silicate melts, are typically performed at $r > 0.02$ MPa/s (e.g., Mourtada-Bonnefoi and Laporte 2004; Cichy et al. 2011; Gondé et al. 2011), while in natural systems r is often < 0.02 MPa/s, depending on the eruptive style (e.g., Cashman 2004). Additionally, the experimental data available in literature to model bubble formation and growth are limited to rhyolitic melt compositions (e.g., Mourtada-Bonnefoi and Laporte 1999; 2002; 2004; Mangan and Sisson 2000; Mangan et al. 2004a; Hamada et al. 2010; Cichy et al. 2011; Gondé et al. 2011), while no information on the behavior of more mafic or depolymerized melts exists.

In this study, continuous decompression experiments were carried out to explore the bubble nucleation and growth in an andesitic melt and the results are compared to rhyolitic melts. The experimental approach chosen in this study simulates the formation of bubbles in an initially bubble- and crystal-free melt, thus enabling the interpretation of homogeneous bubble nucleation. The compiled experiments cover a wide range of r (0.0005 to 0.1 MPa/s). We demonstrate that the decompression path (continuous decompression vs. multi-step decompression) and the initial H_2O contents (H_2O-saturated vs. H_2O-undersaturated) are crucial parameters for the interpretation of bubble number densities.

EXPERIMENTAL PROCEDURE AND ANALYTICAL METHOD

Experimental procedure

In order to investigate the effect of r and t_A on bubble formation and on bubble number densities (*BND*; i.e., the number of bubbles per unit volume) in andesitic melts, the distribution of bubbles in selected experimental products from a previous study by on sulfur distribution between melts and fluids (Fiege et al. 2014) has been investigated.

The experimental strategy applied by Fiege et al. (2014) was as follows: In the *first step*, a synthetic anhydrous glass with a composition corresponding to the Krakatau andesite (Mandeville et al. 1996) was prepared by melting a mixture of oxide and carbonate powders for 2 h in a $Pt_{90}Rh_{10}$ crucible at 1600°C and 1 atm. The melt was quenched to a glass in a water bath, ground and melted again to improve the homogeneity. The composition of the anhydrous andesitic glass is listed in Table 1. In the *second step*, hydrous sulfur-bearing glasses were synthesized at high pressure (~500 MPa; uncertainty of the pressure transducer: ±5 MPa) and high temperature (~1030°C) under fluid absent conditions in internally heated pressure vessels (IHPV). The syntheses were carried out in Au capsules. Glass powder and variable amounts of gypsum powder ($Ca[SO_4]\times 2H_2O$) were mixed thoroughly in an agate mortar. The powder mixture and required amounts of deionized H_2O (H_2O source) were filled stepwise into the Au capsule and were compacted using a piston and a hammer to minimize entrapped air. In some experiments, a 10 wt% HCl aqueous solution was also added to prepare Cl-bearing glasses. The *third step* included the isothermal decompression experiments, conducted in IHPV at a temperature (T) of 1030°C and QFM+0.8 to QFM+1.8.. Ground powder of the synthesized H_2O-S±Cl-bearing starting glass was loaded into gold capsule, compressed to minimized entrapped air, crimped flat and welded shut. This technique produces almost cylindrical melt pools, which minimizes wall effects and allows the expansion of the loaded material during decompression. Prior to decompression, the samples were annealed for ~5 min at a constant pressure (P) of ~400 MPa. Subsequently, pressure was released continuously from 400 MPa to 70 MPa at different rates (r), varying from 0.0005 to 0.1 MPa/s. After the decompression, samples were either rapidly quenched (following the method described by Berndt et al. 2002) to preserve strongly non-equilibrium conditions or were annealed for various times (t_A) at final P and T before quenching in order to approach near-equilibrium conditions for the distribution of volatiles (H_2O, S and Cl)

between melt and fluid. As reported in previous studies on andesitic melts (e.g., King and Holloway 2002; Botcharnikov et al. 2006), the estimated cooling rate of about 150°C/s obtained by applying the rapid quench technique (Berndt et al. 2002) is sufficient for our research purposes.

The experiments selected for the investigation of *BND* are characterized by starting glasses with similar initial water (H_2O) contents of about 6.5 wt%, while their initial sulfur contents are ranging from ~140 to ~1050 ppm and chlorine is varying from 0 to ~1000 ppm. The initial concentrations of H_2O, S and Cl in the starting glasses are given in Table 2 and details on the experimental series GYClA, GYMClA, QFMA and QFMClA as well as on the methods used for the characterization of the volatile concentrations in the starting glasses [electron microprobe (EMP), IR spectroscopy, Karl Fischer titration] are given in Fiege et al. (2014). Solubility experiments of Botcharnikov et al. (2006) indicate that the H_2O solubility in andesitic melts at our starting conditions of ~400 MPa and 1030°C is higher than 6.6 wt%. This is also confirmed by the model of Burnham (1979), which predicts a H_2O solubility of 7.2 wt% for the investigated andesitic melt composition at 400 MPa and 1030°C. The effect of small amounts of S and Cl in the melt on H_2O solubility is presumably negligible (Webster et al. 2009). Moreover, BSE images of the starting glasses as well as of test runs which were immediately quenched after short annealing (~5 to ~10 min) at 1030°C and 400 MPa without decompression show no bubbles. Hence, we conclude that no fluid phase was present prior to decompression as well as within the first tenths of MPa of *P* release. The experimental series QFMA and QFMClA (0.0005 to 0.1 MPa/s; t_A = 0 h; Table 2) were chosen to explore the influence of *r* on *BND*, while series GYClA and GYMClA (0.1 MPa/s; t_A = 0 to ~72 h) were selected to evaluate possible changes in vesiculation processes during annealing after a fast decompression (0.1 MPa/s). The fO_2 of these

experiments was adjusted to ~QFM+0.8 (QFMA and QFMClA) or ~QFM+1.8 (GYClA and GYMClA).

Estimation of bubble number densities (*BND*)

Three BSE images (collected using EMP) of the experimental products were analyzed to characterize bubble size and distribution, using the public computer program ImageJ (http://rsb.info.nih.gov/ij/). The geometric information derived from ImageJ analyses was used to estimate the *BND* of the samples, following the method of Noguchi et al. (2008) with a procedure already applied by Cichy et al. (2011) and Nowak et al. (2011).

The ImageJ software allows us to determine, e.g., total area, average size, area fraction as well as width and length of individual bubbles. Moreover, the (average) minor and major axes as well as the angle of the ellipsoid fitted to the bubbles are automatically calculated and used for subsequent *BND* estimations. As ImageJ analyses provide only 2D bubble size information, the estimation of the *BND* involves as a final step a 3D correction using the CSD-Corrections 1.4 software (http://depcom.uqac.ca/~mhiggins/csdcorrections.html). The methods used in CSD-Corrections 1.4 are described by Higgins (2000, 2002) and Higgins and Chandrasekharam (2007). For the 3D correction, the roundness factor calculated by ImageJ, ranging from 0.6 to 0.9, was applied while the aspect ratio was set to 1.0 - 1.1 - 1.2 (short axis - intermediate axis - long axis).

Noteworthy, the BSE images were taken at different magnifications and from different locations of the samples, which minimizes possible truncation effects (for details see section "Accuracy of the *BND* estimation" and, e.g., Armienti 2008). The image sizes are ranging between ~300 × ~220 µm and ~2500 × ~1850 µm (resolution: ~0.5 to ~2.5 µm/pixel, respectively). We have chosen to process BSE images rather than reflected-light microscopic

images for our *BND* analyses because BSE images show a higher contrast between bubbles and melt.

Table 1

RESULTS

Figure 1 shows a typical microscopic image of a partially degassed andesitic glass (GYClA-3). The size of the bubbles ranges from a few microns up to ~80 μm; a typical feature of fast decompressed (~0.1 MPa/s) samples with 0 to ~2 h of annealing time at final *P*-*T* conditions. The analyses of BSE images indicate that the amount of bubbles decreases while the size of bubbles increases with decreasing *r* from 0.1 to 0.0005 MPa/s (e.g., QFMClA series; Fig. 2). A comparable trend has been observed with increasing t_A after fast decompression (~0.1 MPa/s; e.g., GYMClA; Fig. 3). The bubbles appear often elongated and show a preferred orientation (flow structures) – especially in experiments with low *r* (< 0.02 MPa/s) and/or long term annealing after decompression (t_A > 5 h) – indicating that convection may have occurred during the experimental runs. No significant influence of small variations in the S and/or Cl content in the system on the *BND* was detected (see Fig. 4).

Figure 1, 2, 3 and 4

Accuracy of the *BND* estimation

As mentioned previously, the method applied for the estimation of the *BND* may result in truncation effects which can affect *BND* values significantly (e.g., Armienti 2008). Such truncation effects either arise from the resolution of the BSE image (left-hand truncation) or from

the image size (right-hand truncation). In case of left-hand truncation, the number of bubbles with a size close to the resolution limit is reduced. However, the resolution of the BSE images used in this study was found to be sufficient to detect bubbles with a diameter of ≥ 1 μm, while microscopic investigations indicate that the amount of bubbles with a diameter < 1 μm is negligible. Thus, a reduction of the number of the smallest bubbles is unlikely in our case, implying that left-hand truncation can be ruled out. Right-hand truncation effects occur when the largest bubbles in the sample are excluded or are underrepresented in the analyzed area of the sample. In bubble size distribution (BSD) plots, this would result in a flattening of the size distribution to nearly horizontal trends at large sizes. However, such trends are not observed in the *BSD* plots, implying that right-hand truncation is unlikely (see Fig. A.1 in the appendix, showing *BSD* plots of selected samples).

Another source of error is the treatment of bubbles which are located partly outside the area covered by the image. To account for this problem, *BND* values were estimated using two approaches. In the first approach, bubbles which were cut at the image edge were excluded from the calculation. In the second approach, the area of the bubbles visible in the image was included in the calculation. The *BND* values derived from these two procedures differ by less than 0.12 log. The *BND* values obtained from the three different images of one sample, taken at different magnifications and from different locations, differ typically by < 0.8 log units, indicating a quite homogeneous distribution of the bubbles within the samples. The average *BND* values of all six analyses (i.e., 3 images at different magnifications and locations on the sample; bubbles at the edges included or excluded) are listed in Table 2.

Table 2

190 **Influence of r and t_A on *BND***

191 The *BND* data of experiments conducted at different r and with immediate quenching at
192 final P (t_A = 0 h) are shown in Figures 4a and 5. A roughly linear increase of log(*BND* × mm^3)
193 with log(r × s/MPa) is indicated by the data obtained in this study for hydrous, but initially not
194 volatile-saturated andesitic melts. Figure 5 shows that the *BND* values determined in previous
195 experimental studies (e.g., Mangan and Sisson 2000; Mourtada-Bonnefoi and Laporte 2004;
196 Hamada et al. 2010) on homogeneous nucleation in CO_2-free, H_2O-saturated rhyolitic systems at
197 700 to 900°C are typically more than 1 log unit lower than those obtained in this study. *BND*
198 values determined by Gondé et al. (2011) for homogeneous nucleation in H_2O-undersaturated
199 rhyolitic melts at 730 to 1000°C and for r ranging from 0.06 to 2.3 MPa/s show no clear trend
200 and have to be interpreted with caution due to the H_2O loss during their experiments as already
201 mentioned by the authors. However, the data obtained by Gondé et al. (2011) for a r of 40 to 50
202 MPa/s seem to be in good agreement with other experimental results on H_2O-saturated rhyolitic
203 systems (e.g., Hamada et al. 2010; see Fig. 5). Changes in bulk Cl and S contents as well as slight
204 variations in fO_2, varying from ~QFM+0.8 to ~QFM+1.8, have no significant effect on the
205 decompression-induced bubble formation in the studied andesitic melts.

206 The influence of t_A on *BND* has been studied at QFM+1.8 (experimental series GYClA
207 and GYMClA; *BND* values listed in Table 2) and at a constant r of ~0.1 MPa/s. Figure 4b
208 indicates that log(*BND* × mm^3) decreases by 1 log unit or more within the first ~5 h of annealing
209 after decompression. *BND* values obtained from one experimental series with t_A = 5 h and t_A = 72
210 h are identical within error, and it can be concluded that annealing of more than 5 h after
211 decompression has a minor effect on *BND*.

212

213

DISCUSSION

Role of microlites and decompression path on bubble nucleation

In Figure 4a the *BND* data of this study for *r* ranging from 0.0005 to 0.1 MPa/s and $t_A = 0$ h are compared to the experimental results of Cichy et al. (2011). Cichy et al. (2011) investigated the vesiculation in a rhyodacitic system induced by a decompression from 300 to 50 MPa at 850°C (*r* ranging from 0.0002 to 20 MPa/s). It is emphasized that the differences in *T* should have a negligible effect on *BND* at given *r* (see Fig. 5 and Hamada et al. 2010). As mentioned above, a roughly linear increase of $\log(BND \times mm^3)$ with $\log(r \times s/MPa)$ is indicated by our experimental series QFMA and QFMClA (Fig. 4a; Table 2). In contrast, Cichy et al. (2011) observed a minimum of $\log(BND \times mm^3)$ at $r \approx 0.02$ MPa/s. Noteworthy, the experiments of Cichy et al. (2011) were conducted to investigate the combination of simultaneous decompression-induced degassing and crystallization. The samples before decompression contained significant amounts of crystalline phases (including Fe-Ti microlites). Thus, heterogeneous bubble nucleation processes were studied by Cichy et al. (2011), while homogeneous nucleation is assumed for our experiments. However, the results of Mangan and Sisson (2000) indicate that *BND* in experiments with heterogeneous nucleation are comparable to the values of homogenous nucleation at given *r*. Mangan and Sisson (2005) noted that the presence or absence of heterogeneity in the melt dictates the supersaturation pressure ΔP, while the nucleation rate (homogenous or heterogeneous) is mainly influenced by *r*. The microlite number densities (*MND*) determined by Cichy et al. (2011) do not show any clear dependence on *r* ($MND \approx 10^{5.5}$ mm^{-3} in the range of 0.0002 MPa/s to 20 MPa/s), indicating that changes in nucleation style (homogenous vs. heterogeneous), cannot explain the *BND* minimum at $r \approx 0.02$ MPa/s observed by Cichy et al. (2011). Cichy et al. (2011) calculated *MND* values either for plagioclase only or for all other phases together, such as amphibole, pyroxene and oxides.

238 However, considering that Fe-Ti-oxides are very important bubble nucleation sites (Hurwitz and
239 Navon 1994), calculating *MND* for Fe-Ti-oxides only may provide useful information to interpret
240 the *BND* data of Cichy et al. (2011).

241 Cichy et al. (2011) applied a multi-step decompression technique to conduct experiments
242 with $r \leq 0.01$ MPa/s, implying that pressure was released stepwise over the whole run duration
243 (typical decompression steps ranged between 8.4 to 40 MPa). Nowak et al. (2011) revealed a
244 significant influence of the decompression style on homogeneous bubble nucleation in the same
245 rhyodacitic melt at T above the liquidus (1050°C). The authors show that the multi-step
246 decompression technique leads to *BND* values which are more than one log unit higher than those
247 obtained for continuous decompression at given r. *BND* values determined by Nowak et al.
248 (2011) for single-step decompression experiment are even higher. Thus, the differences between
249 our *BND* data and the multi-step decompression data of Cichy et al. (2011; see Fig. 4a) are
250 consistent with the observations made by Nowak et al. (2011), and the non-linear trend found by
251 Cichy et al. (2011) can probably be assigned to variations in the decompression style. A
252 comparison of our data with *BND* values determined by Gardner and Denis (2004) and Gardner
253 (2007) for heterogeneous bubble nucleation in CO_2-free, H_2O-saturated rhyolitic melts at 550 to
254 800°C, using single-step decompression technique, confirms this hypothesis. For instance,
255 Gardner and Denis (2004) calculated *BND* values of $10^{4.7}$ to $10^{5.0}$ mm^{-3} at $r \approx 0.007$ MPa/s, while
256 we observed about one log unit lower *BND* values ranging from $10^{3.4}$ to $10^{4.0}$ mm^{-3} for a slightly
257 higher r of about 0.01 MPa/s. However, at $r \approx 0.1$ MPa/s Gardner and Denis (2004) and Gardner
258 (2007) estimated *BND* values of $10^{4.6}$ to $10^{5.2}$ mm^{-3}, while we determined *BND* values ranging
259 from $10^{4.2}$ to $10^{4.9}$ mm^{-3} for similar r, indicating that the influence of decompression style on *BND*
260 may decrease with increasing r.

The differences in bubble nucleation observed between continuous decompression and multi-step decompression may arise from a high ΔP induced by instantaneous P drops of 50 MPa during multi-step decompression experiment, leading to a predominance of bubble nucleation (Nowak et al. 2011). With respect to continuous decompression, as stated by Nowak et al. (2011), nucleation may require a certain ΔP and, thus, bubble growth will dominate over nucleation processes upon further continuous decompression caused by favorable energetics (e.g., review of Sparks et al. 1994; Nowak et al. 2011). Nevertheless, the increase of $\log(BND \times mm^3)$ with decreasing multi-step decompression rate at $r < 0.01$ MPa/s observed by Cichy et al. (2011) needs to be clarified by further investigations.

Figure 5

Bubble formation during magma storage after a fast ascent

The observed strong decrease of $\log(BND \times mm^3)$ with increasing t_A (series GYClA and GYMClA; see Fig. 4b) is probably linked to the very fast decompression ($r \sim 0.1$ MPa/s). It is assumed that a fast decompression of the andesitic melt leads to a high supersaturation pressure (ΔP). Thus, the gas (H_2O-S±Cl) pressure in the melt is significantly larger than the ambient P in the vessel (Sparks et al. 1994). Furthermore, as a consequence of the high ΔP, the critical radius size of the bubble embryo is lowered, leading to the domination of bubble nucleation over bubble growth and/or coalescence upon decompression. The resulting significant decrease of BND by about 1 log unit within the first few hours of annealing indicates that coalescence and/or bubble growth become more important than nucleation.

Evidence of bubbles coalescence is preserved in our quenched experimental end-products and can be seen in the BSE images of our series GYMClA in Figure 3. Common bubble

coalescence structures such as interpenetration shapes, dimples or flattened inter-bubble melt films (Castro et al., 2012) can be observed especially in experiments with short annealing times (Fig. 3a-d with t_A of 0 and 1h). In contrast, at longer t_A (t_A=5h; see Fig. 3e and 3f), such bubble shapes were not observed, and only few large bubbles (diameters typically > 200μm) are preserved in the quenched glass. This indicates that most previously small-sized vesicles merged together within t_A of 1 and 5 h to form larger individuals, which may even have migrated to the capsule wall.

The determination of the volatile concentrations in the melt after decompression is also useful to interpret bubble growth and coalescence upon further annealing. The volatile contents (H_2O, S, Cl) were determined by Fiege et al. (2014) using IR spectroscopy (H_2O content) as well as EMP analyses (S, Cl) and the data are given in their Table 2. Figure 6 shows that the H_2O concentrations of the partially decompressed andesitic melts remain nearly constant during annealing at final *P-T* conditions. The small variations in H_2O (3.56 to 3.84 wt%; except GYMClA-4: 1.98 wt%) concentrations in the melt are independent of t_A (and r) and within uncertainty of the determination (see Fig. 6b, and 6f). The low H_2O concentration measured by Fiege et al. (2014) in the glass of sample GYMClA-4 can possibly be explained by the loss of small amounts of volatiles from the capsule at the end of the experiments, though no clear evidence for such a leakage were observed. By contrast, minor amounts of S and Cl are still released from the melt to the fluid phase within the first hour of annealing after decompression (e.g., GYClA series: S_{melt} decreases from ~180 ppm to 90 ppm upon annealing; see Fig. 6e). Nevertheless, Figure 6 clearly shows that most of the volatiles have already been exsolved upon decompression. Thus, in agreement with observations made on BSE images (see previous paragraph), it is proposed that coalescence dominates over bubble growth upon further annealing at final *P-T* conditions. However, Lautze et al. (2011) noted that diffusive coarsening, also known

as Ostwald ripening, should be the dominant mechanism leading to decreasing *BND* with increasing t_A. Hence, in addition to volatile diffusion, other processes (e.g., convection fluxes) may have influenced the bubble formation in our decompression experiments.

Figure 6

Comparison of experimental data with the model of Toramaru (2006) and with previous results

Toramaru (2006) developed a model to estimate *r* based on *BND* data of natural pumices. Our experimental data are used to test this decompression-rate-meter for andesitic systems. The following equation, based on the numerical simulations of Toramaru (1995; 2006) and provided by Hamada et al. (2010), was applied to estimate the *BND* for diffusion-controlled bubble nucleation in andesitic melts:

$$BND \approx 34 \cdot C_{SAT} \cdot \left(\frac{16 \cdot \pi \cdot \sigma_{LB}^3}{3 \cdot k \cdot T \cdot P_{SAT}^2} \right)^{-2} \cdot \left(\frac{\Omega_L \cdot P_{SAT}}{k \cdot T} \right)^{-\frac{1}{4}} \cdot \left(\frac{P_{SAT}^2 \cdot k \cdot T \cdot C_{SAT} \cdot D_{H2O}}{4 \cdot \sigma_{LB}^2 \cdot r} \right)^{-\frac{3}{2}} \quad (1)$$

where C_{SAT} is the H_2O content at saturation pressure expressed as the number of H_2O-molecules per unit volume of liquid, σ_{LB} is the surface tension of the bubble-liquid interface in N/m, *k* is the Boltzmann constant (1.38×10^{-23} J/K), *T* is the temperature in K, P_{SAT} is the H_2O saturation pressure in Pa, Ω_L is the molecular volume of H_2O in the liquid (fixed to 3×10^{-29} m^3; Toramaru 1989; Hamada et al. 2010), D_{H2O} is the H_2O diffusivity in the melt in m^2/s, and *r* is the decompression rate in Pa/s.

In a first approximation, P_{SAT} is assumed to be the P at which a H_2O activity [$a(H_2O)$] of ~1 is reached in the andesitic system upon decompression. Thus, P_{SAT} strongly depends on the initial H_2O content in the melt (here: 6.3 to 6.6 wt%). Assuming that the S and Cl contents in the andesitic system do not affect significantly the water solubility, P_{SAT} is estimated to range between 3.04×10^8 Pa for ~6.3 wt% H_2O initial and 3.31×10^8 Pa for ~6.6 wt% H_2O initial at 1030°C (see Table A.1 in the appendix) using the model of Burnham (1979). This assumption is confirmed by experiments of Webster et al. (2009) indicating that S (~0.02 to ~0.13 wt%) and Cl (~0.16 to ~0.84 wt%) have a minor effect on the H_2O solubility at 200 MPa and ~900 to ~1000°C in phonolitic systems, as well as by Fig. 6a and 6b, which clearly show that the final H_2O contents in the decompressed glasses are largely independent of the bulk S and Cl concentrations. Subsequently, C_{SAT} at P_{SAT} is calculated to range between 4.67×10^{27} and 4.90×10^{27} m^{-3} for ~6.3 to ~6.6 wt% H_2O using the model of Ochs and Lange (1999) to estimate the density of the melt (ρ_{melt}) at P_{SAT} and 1030°C (see Table A.1 in the appendix). Furthermore, we have used the relationship provided by Behrens et al. (2004) for the estimation of the H_2O diffusivity in dacitic melts as a function of T and H_2O content in the melt in order to calculate D_{H2O}. Assuming an initial H_2O content in the melt of 6.5 wt% (prior to decompression) and a final H_2O content of 3.6 wt% (after decompression; see also Fiege et al., 2014), D_{H2O} is estimated to decrease from 2.03×10^{-11} m^2/s to 1.12×10^{-11} m^2/s during the decompression process. An average D_{H2O} value of 1.58×10^{-11} m^2/s has been used for our *BND* calculations.

We have chosen the equation of Behrens et al. (2004) proposed for dacitic melts rather than that proposed for an andesitic melt because the melt composition used in this study (Krakatau andesite) is closer to the dacite than to the andesite. D_{H2O} estimated using the relationship for andesitic systems provided by Behrens et al. (2004) or using the general model developed by Zhang and Ni (2010) would be ~2.5 to ~4.8 times higher than the D_{H2O} of a dacitic

355 melt, which would result in a decrease of the *BND* values by ~0.6 to ~0.8 log units lower at given
356 *r*.

357 The value of σ_{LB} is estimated using the following equation (e.g., Hirth et al. 1970; Blander
358 and Katz 1975; Hurwitz and Navon 1994; Mangan and Sisson 2005; Gardner and Ketcham
359 2011):
360

361 $$J = \frac{2 \cdot n_0^2 \cdot \Omega_L \cdot D_{H2O} \cdot \left[\sigma_{LB} / (k \cdot T)\right]^{1/2}}{a_0} \cdot \exp\left[\frac{-16 \cdot \pi \cdot \sigma_{LB}^3}{3 \cdot k \cdot T \cdot \Delta P^2}\right] \quad (2)$$

362

363 where *J* is the nucleation rate calculated by dividing the determined *BND* by the time
364 allowed for nucleaction (t_N; see, e.g., Gardner and Ketcham 2011). Here, t_N is the sum of the
365 duration of the decompression and t_A. The number density of dissolved water molecules n_0 is
366 estimated using the concentration of H_2O molecules measured by IR spectroscopy in the starting
367 glasses and the density of the starting glasses ρ_{glass}. The values for ρ_{glass} are estimated from the
368 glass composition using the Gladstone-Dale rule (Gladstone and Dale 1863; see also Mandeville
369 et al. 2002). The IR measurements are described in detail in Fiege et al. (2014) and the
370 determined concentrations for molecular H_2O [$c(H_2O)$] and OH groups [$c(OH)$] are given in
371 Table A.1 in the appendix. The mean distance between dissolved water molecules a_0 is calculated
372 assuming the stereological definition $a_0 = 0.667\ (d / V_{frac})$ from Russ (1986) in which *d* is the
373 diameter of a water molecule (3.7×10^{-10} m) and V_{frac} is the volume fraction of water molecules
374 in the melt. ΔP is the critical supersaturation pressure required to overcome the kinetic barrier to
375 nucleation at a specific *T* and H_2O content (Mangan and Sisson 2005). ΔP cannot be determined
376 directly from our experiments. However, the lower viscosity of the studied andesitic melts when

compared, for instance, to rhyodacitic melts should lead to a lower surface tension and a lower ΔP. This is in agreement with the results of Mangan and Sisson (2005), which show a remarkable decrease of σ_{LB} with the addition of mafic components (e.g., CaO, FeO_{total}, MgO). Thus, we suggest that the ΔP of 60 MPa determined by Mangan and Sisson (2005) for rhyodacitic melts (~69 wt% SiO_2; ~5 wt% initial H_2O) at 1000°C should represent an upper limit for the ΔP of the studied composition. Preliminary experimental data of Masotta et al. (2013) indicate that ΔP may be < 20 MPa in andesitic melts and, thus, σ_{LB} was estimated to range from 0.028 to 0.063 N/m (see Table 2) in our experiments on evolved andesitic compositions, assuming a ΔP of 20 and 60 MPa, respectively. These upper and lower σ_{LB} values are applied to predict *BND*-trends for the studied andesitic melt at 1030°C, assuming an average initial H_2O content of 6.5 wt% and an average ρ_{melt} of 2.225 g/cm^3 (see Fig. 5). Figure 5 shows clearly that log(*BND* × mm^3) obtained from experiments of this study, which were quenched directly after continuous decompression, increases linearly with log(r × s/MPa), being in good agreement with the calculated trend using the Toramaru (2006) model. The experimental data for the initially H_2O-undersaturated andesitic melts of this study indicate a similar slope as predicted by the Toramaru (2006) model; however, the *BND* values of the experiments are about 0.5 to 1.5 log unit higher than those of the modeled trends which were calculated assuming a σ_{LB} of 0.028 or 0.063 N/m. Experimental data on homogeneous nucleation in CO_2-free rhyolitic systems obtained by Mangan and Sisson (2000), Mourtada-Bonnefoi and Laporte (2004), Hamada et al. (2010) as well as Gondé et al. (2011) at 700 to 1000°C are plotted in Figure 5 for comparison. CO_2-bearing experiments are not considered as CO_2 presumably affects bubble formation to a significant extent (see , e.g., Cichy et al. 2011). The data for homogeneous nucleation during decompression of initially H_2O-saturated rhyolitic systems (Mangan and Sisson 2000; Mourtada-Bonnefoi and

Laporte 2004; Hamada et al. 2010) show *BND* values which are about 1 to 2 log units lower at given *r* than values determined in this study for initially H_2O-undersaturated andesitic systems. These previously published *BND* data for H_2O-saturated rhyolitic systems indicate even slightly lower *BND* values than predicted by the Toramaru (2006) model for rhyolitic compositions at 800°C (σ_{LB} = 0.08 N/m; see Fig. 5). Noteworthy, the large scatter of most results published by Gondé et al. (2011) does not allow a clear interpretation of their data. Considering that *T* has most likely a minor effect on decompression-induced bubble nucleation (see Fig. 5 and Hamada et al. 2010), the experimental results of andesitic and rhyolitic systems indicate that the compositional effect on bubble formation is more pronounced than predicted by the Toramaru (2006) model using equation 2 for the estimation of σ_{LB}. For instance, Figure 5 shows that the Toramaru (2006) model may be able to predict our data if a low σ_{LB} of ~0.015 N/m is assumed. On the other hand, Pichavant et al. (2013) determined a σ_{LB} of 0.18 N/m for H_2O-CO_2-bearing basaltic melts at 1140 to 1180°C indicating that σ_{LB} can also be significantly higher in mafic melts than suggested by the data of Mangan and Sisson (2005). However, the high σ_{LB} values found by Pichavant et al. (2013) are probably in part related to the positive correlation between *T* and σ_{LB} (e.g., Bagdassarov et al 2000; Mangan and Sisson 2005) and/or to the influence of CO_2 on bubble formation (e.g., Mourtada-Bonnefoi and Laporte 2002).

Strictly, the dependence of *BND* on *r* reflects the influence of the degree of volatile supersaturation on bubble formation and is a non-linear function of changing total *P* (see equation 1, and Mangan et al. 2004b; Mangan and Sisson 2005). Considering that all variables except ΔP required for the calculation of σ_{LB} using equation 2 are well constrained and/or have a negligible influence on σ_{LB} (e.g., P_{SAT}), the ΔP of the investigated andesitic melt is possibly lower than 20 MPa. However, very low ΔP (< 8 MPa) are required in order to obtain a σ_{LB} of about

0.015 N/m using equation 2. Such low values for ΔP are quite unlikely considering that we studied an evolved andesitic melt which does not show strong differences in major element composition when compared to the rhyodacite of Mangan and Sisson (2005). Here, it is important to emphasize that equation 1 and 2 do not account for the influence of volatiles other than H_2O on bubble formation. Although the $\log(BND \times mm^3)$ values determined for experiments directly quenched after fast decompression at r = 0.1 MPa/s (GYClA-1, GYMClA-1, QFMA-1; QFMClA-1) are similar (see Table 2), indicating that the variation of the bulk S (~140 to ~1000 ppm) and Cl (0 to ~1000 ppm) content may have a minor effect on bubble formation, the presence of these two volatile may play an important role. In addition, the fluid phase released by the andesitic melt upon decompression contains also significant amounts of charge balancing cations like, for instance, Na^+ and/or Ca^{2+} (see e.g., Zajacz et al. 2012). Hence, the diffusivity of S, Cl, and alkalis in the melt (D_S, D_{Cl}, $D_{alkalis}$) should be included in an updated approach for the calculation of *BND* as a function of r (equation 1) and for the calculation of σ_{LB} as a function of J and ΔP (equation 2). This is justified by the analysis of Figure 6, showing that minor amounts of S and Cl are still released from the melt to the fluid phase during the first hour of annealing after fast decompression (0.1 MPa/s).

The H_2O-activitiy [$a(H_2O)$] prevailing in the melt prior to decompression may provide another explanation for the strong deviation observed between our data for andesitic systems and the modeled trend. Noteworthy, our data as well as the problematic dataset of Gondé et al. (2011) are obtained for melts which are not saturated in H_2O before decompression, which is in contrast to all other literature data shown in Figure 5. Gondé et al. (2011) proposed that H_2O-understaturated melts could explain *BND* values which are several log units higher when compared to H_2O-saturated melts. The presence of a free-fluid phase prior to decompression, e.g., in the form of microbubble nuclei, can possibly explain the lower *BND* values derived in initially

447 H_2O-saturated experiments due to dominating bubble growth over bubble nucleation upon
448 decompression. However, this would imply that the H_2O-saturated starting materials of Mangan
449 and Sisson (2000), Mourtada-Bonnefoi and Laporte (2004) and Hamada et al. (2010) contain
450 microbubbles prior to decompression without being mentioned by the authors, which is quite
451 unlikely. Presuming that H_2O-activity prior to decompression plays an important role, and
452 considering that magmatic systems are often not H_2O-saturated before an eruption (e.g., Hervig et
453 al. 1989; Gardner et al. 1995), the commonly much higher *BND* values determined for natural
454 pumices when compared to most experimental data (Hamada et al. 2010) can, at least in part, be
455 explained by the experimental strategy applied in most previous works; i.e., initially H_2O-
456 saturated melts.

457 In conclusion, the most plausible explanation for the discrepancies observed between our
458 dataset for a H_2O+S±Cl-bearing andesitic system and the trend(s) predicted by the Toramaru
459 (2006) model is that equation 1 (Toramaru (2006) model) and 2 (estimation of σ_{LB}) are
460 inadequate to predict decompression-induced bubble nucleation within initially H_2O+S±Cl-
461 undersaturated systems because, e.g., D_S, D_{Cl}, $D_{alkalis}$, and a(H_2O) are not considered.

462

463 **IMPLICATIONS FOR NATURAL SYSTEMS**

464 This study presents for the first time experimental data on bubble formation in andesitic
465 systems during continuous decompression, while previous experimental investigations (using
466 comparable techniques) exclusively focused on rhyolitic systems. Two main results are of
467 importance to the *BND* interpretation of pumices formed, for instance, during explosive Plinian
468 eruptions and can help to evaluate existing bubble nucleation models.

First, the strong influence of t_A on *BND* mentioned above (Fig. 4b) indicates that a good knowledge of possible storage times during magma ascent is required to interpret magma ascent rates on the basis of natural pumice samples.

Second, our data show that anhydrous melt composition is crucial to model bubble formation. Considering that the composition of the studied dacitic andesite (~65 wt% bulk SiO_2 in the anhydrous starting glass) is similar to the composition of the material erupted by some hazardous volcanic eruptions such as the 1883 eruption of Krakatau volcano (~64 to 69 wt% SiO_2 in the almost dry bulk samples, ~60 to ~72 wt% in the matrix glasses and glass inclusions; Mandeville et al. 1996) our data are important for our understanding of the vesiculation in the volcanic ejecta of this type of volcanism. Ascent rates estimated on the basis of *BND* in dacitic to andesitic volcanic ejecta may be overestimated by about an order of magnitude if the model of Toramaru (2006) is used to account for compositional variations. Thus, the interpretation of the vesiculation of tephritic samples, which cover commonly a wide range of compositions (SiO_2 content of glass shards of the Mariana tephra ranges from ~53 to ~67 wt%; Straub 1995) needs experimental calibrations for appropriate composition. A larger dataset, accounting for variations in major elements as well as in initial volatile contents ($H_2O \pm CO_2 \pm S \pm Cl$) would be helpful to calibrate the Toramaru (2006) model. This improved "decompression-meter" would allow us to obtain detailed insights on how (fast) magma travels from a deep reservoir to the surface based on vesiculated samples.

ACKNOWLEDGEMENTS

This project was supported by the German Science Foundation (BE1720/25-1). We would like to thank Harald Behrens (scientific discussions), Eric Wolff (electron microprobe) and Otto Dietrich (sample preparation). The valuable comments of the journal editor F. Castro as well as

493 of the reviewers M. Mangan, C. Martel, and A. Toramaru have significantly improved the quality
494 of this manuscript.

495

496 **REFERENCES**

497 Armienti, P. (2008) Decryption of igneous rock textures: crystal size distribution tools. In K.D.
498 Putirka and F.J. Tepley III, Eds., Minerals, Inclusions and Volcanic Processes, 69, p. 623–649.
499 Reviews in Mineralogy and Geochemistry, Mineralogical Society of America, Chantilly,
500 Virginia.

501 Bagdassarov, N., Dorfman, A., and Dingwell, D.B. (2000) Effect of alkalis, phosphorus, and
502 water on the surface tension of haplogranite melt. American Mineralogist, 85, 33-40.

503 Behrens, H., Zhang, Y.X., and Xu, Z.G. (2004) H_2O diffusion in dacitic and andesitic melts.
504 Geochimica et Cosmochimica Acta, 68, 5139-5150.

505 Berndt, J., Liebske, C., Holtz, F., Freise, M., Nowak, M., Ziegenbein, D., Hurkuck, W., and
506 Koepke, J. (2002) A combined rapid-quench and H_2-membrane setup for internally heated
507 pressure vessels: Description and application for water solubility in basaltic melts. American
508 Mineralogist, 87, 1717-1726.

509 Blander, M., and Katz, J.L. (1975) Bubble nucleation in liquids. American Institute of Chemical
510 Engineers Journal, 21, 833-848.

511 Botcharnikov, R.E., Behrens, H., and Holtz, F. (2006) Solubility and speciation of C-0-H fluids
512 in andesitic melt at T=1100-1300 degrees C and P=200 and 500MPa. Chemical Geology, 229,
513 125-143.

514 Burnham, C.W. (1979) Magmas and hydrothermal fluids. In H. L. Barns, Ed., Geochemistry of
515 hydrothermal ore deposits, p. 71-136. John Willey and Sons, New York.

Cashman, K.V. (2004) Volatile controls on magma ascent and eruption. In R.S.J. Sparks and C.J. Hawkesworth, Eds., The State of the Planet: Frontiers and Challenges in Geophysics, 150, p. 109-124. Geophysical Monograph series, American Geophysical Union, Washington.

Castro, J.M., Burgisser, A., Schipper, C.I., and Mancini, S. (2012) Mechanisms of bubble coalescence in silicic magmas. Bulletin of Volcanology, 74, 2339-2352.

Cichy, S.B., Botcharnikov, R.E., Holtz, F., and Behrens, H. (2011) Vesiculation and Microlite Crystallization Induced by Decompression: a Case Study of the 1991–1995 Mt Unzen Eruption (Japan). Journal of Petrology, 52, 1469-1492.

Fiege, A., Behrens, H., Holtz, F., and Adams, F. (2014) Kinetic vs. thermodynamic control of degassing of H_2O-S±Cl bearing andesitic melts. Geochimica et Cosmochimica Acta, 125, 241-254. (DOI: 10.1016/j.gca.2013.10.012)

Gardner, J.E. (2007) Heterogeneous bubble nucleation in highly viscous silicate melts during instantaneous decompression from high pressure. Chemical Geology, 236, 1-12.

Gardner, J.E., and Denis, M.-H. (2004) Heterogeneous bubble nucleation on Fe-Ti oxide crystals in high-silica rhyolitic melts. Geochimica et Cosmochimica Acta, 68, 3587-3597.

Gardner, J.E., and Ketcham, R.A. (2011) Bubble nucleation in rhyolite and dacite melts: temperature dependence of surface tension. Contributions to Mineralogy and Petrology, 162, 929-943.

Gardner, J.E., Rutherford, M., Carey, S., and Sigurdsson, H. (1995) Experimental constraints on pre-eruptive water contents and changing magma storage prior to explosive eruptions of Mount St Helens volcano. Bulletin of Volcanology, 57, 1-17.

Gladstone, and Dale (1863) Researches on the Refraction, Dispersion, and Sensitiveness of Liquids. Philosophical Transactions of the Royal Society of London, 153, 317-343.

539 Gondé, C., Martel, C., Pichavant, M., and Bureau, H. (2011) In situ bubble vesiculation in silicic
540 magmas. American Mineralogist, 96, 111-124.
541 Hamada, M., Laporte, D., Cluzel, N., Koga, K.T., and Kawamoto, T. (2010) Simulating bubble
542 number density of rhyolitic pumices from Plinian eruptions: constraints from fast
543 decompression experiments. Bulletin of Volcanology, 72, 735-746.
544 Hervig, R.L., Dunbar, N., Westrich, H.R., and Kyle, P.R. (1989) Pre-eruptive water content of
545 rhyolitic magmas as determined by ion microprobe analyses of melt inclusions in phenocrysts.
546 Journal of Volcanology and Geothermal Research, 36, 293-302.
547 Higgins, M.D. (2000) Measurement of crystal size distributions. American Mineralogist, 85,
548 1105-1116.
549 Higgins, M.D. (2002) Closure in crystal size distributions (CSD), verification of CSD
550 calculations, and the significance of CSD fans. American Mineralogist, 87, 171-175.
551 Higgins, M.D., and Chandrasekharam, D. (2007) Nature of Sub-volcanic Magma Chambers,
552 Deccan Province, India: Evidence from Quantitative Textural Analysis of Plagioclase
553 Megacrysts in the Giant Plagioclase Basalts. Journal of Petrology, 48, 885-900.
554 Hirth, J.P., Pound, G.M., and Pierre, G.R.St. (1970) Bubble nucleation. Metallurgical
555 Transactions, 1, 939-945.
556 Hurwitz, S., and Navon, O. (1994) Bubble nucleation in rhyolitic melts: Experiments at high
557 pressure, temperature, and water content. Earth and Planetary Science Letters, 122, 267-280.
558 King, P.L., and Jolloway, J.R. (2002) CO_2 solubility and speciation in intermediate (andesitic)
559 melts: The role of H_2O and composition. Geochimica et Cosmochimica Acta, 66, 1627-1640.
560 Lautze, N., Sisson, T., Mangan, M., and Grove, T. (2011) Segregating gas from melt: an
561 experimental study of the Ostwald ripening of vapor bubbles in magmas. Contributions to
562 Mineralogy and Petrology, 161, 331-347.

563 Mandeville, C.W., Carey, S., and Sigurdsson, H. (1996) Magma mixing, fractional crystallization
564 and volatile degassing during the 1883 eruption of Krakatau volcano, Indonesia. Journal of
565 Volcanology and Geothermal Research, 74, 243-274.
566 Mandeville, C.W., Webster, J.D., Rutherford, M.J., Taylor, B.E., Timbal, A., and Faure, K.
567 (2002) Determination of molar absorptivities for infrared absorption bands of H_2O in andesitic
568 glasses. American Mineralogist, 87, 813-821.
569 Mangan, M., and Sisson, T. (2000) Delayed, disequilibrium degassing in rhyolite magma:
570 decompression experiments and implications for explosive volcanism. Earth and Planetary
571 Science Letters, 183, 441-455.
572 Mangan, M., and Sisson, T. (2005) Evolution of melt-vapor surface tension in silicic volcanic
573 systems: Experiments with hydrous melts. Journal of Geophysical Research, 110, B01202.
574 Mangan, M., Mastin, L., and Sisson, T. (2004a) Gas evolution in eruptive conduits: combining
575 insights from high temperature and pressure decompression experiments with steady-state
576 flow modeling. Journal of Volcanology and Geothermal Research, 129, 23-36.
577 Mangan, M.T., Sisson, T.W., and Hankins, W.B. (2004b) Decompression experiments identify
578 kinetic controls on explosive silicic eruptions. Geophysical Research Letters, 31,
579 L08605.Masotta, M., Ni, H., and Keppler, H. (2013) In-situ observations of bubble growth in
580 basaltic, andesitic and rhyodacitic melts. Abstract V13H-04 presented at 2013 Fall Meeting,
581 San Fransisco, Calif., 9-13 Dec.
582 Mourtada-Bonnefoi, C.C., and Laporte, D. (1999) Experimental study of homogeneous bubble
583 nucleation in rhyolitic magmas. Geophysical Research Letters, 26, 3505-3508.
584 Mourtada-Bonnefoi, C.C., and Laporte, D. (2002) Homogeneous bubble nucleation in rhyolitic
585 magmas: An experimental study of the effect of H_2O and CO_2. Journal of Geophysical
586 Research, 107, ECV 2-1-EVC 2-19.

587 Mourtada-Bonnefoi, C.C., and Laporte, D. (2004) Kinetics of bubble nucleation in a rhyolitic
588 melt: an experimental study of the effect of ascent rate. Earth and Planetary Science Letters,
589 218, 521-537.
590 Noguchi, S., Toramaru, A., and Nakada, S. (2008) Relation between microlite textures and
591 discharge rate during the 1991-1995 eruptions at Unzen, Japan. Journal of Volcanology and
592 Geothermal Research, 175, 141-155.
593 Nowak, M., Cichy, S.B., Botcharnikov, R.E., Walker, N., and Hurkuck, W. (2011) A new type of
594 high-pressure low-flow metering valve for continuous decompression: First experimental
595 results on degassing of rhyodacitic melts. American Mineralogist, 96, 1373-1380.
596 Ochs, F.A., and Lange, R.A. (1999) The Density of Hydrous Magmatic Liquids. Science, 283,
597 1314-1317.
598 Pichavant, M., Carlo, I., Rotolo, S.G., Scaillet, B., Burgisser, A., Gall, N., and Martel, C.(2013)
599 Generation of CO_2-rich melts during basalt magma ascent and degassing. Contributions to
600 Mineralogy and Petrology, 166, 545-561.
601 Russ, J.C. (1986) Practical Stereology, Springer, New York.
602 Sparks, R.S.J., Barclay, J., Jaupart, C., Mader, H.M., and Phillips, J.C. (1994) Physical Aspects
603 of Magma Degassing – I. Experimental and theoretical constraints on vesiculation. In M.R.
604 Carroll and J.R. Holloway, Eds., Volatiles in Magmas, 30, p. 413–445. Reviews in
605 Mineralogy, Chantilly, Virginia.
606 Straub, S.M. (1995) Contrasting compositions of Mariana Trough fallout tephra and Mariana
607 Island arc volcanic: a fractional crystallization link. Bulletin of Volcanology, 57, 403-421.
608 Toramaru, A. (1989) Vesiculation process and bubble size distributions in ascending magmas
609 with constant velocities. Journal of Geophysical Research, 94, 17523-17542.

610 Toramaru, A. (1995) Numerical study of nucleation and growth of bubbles in viscous magmas.
611 Journal of Geophysical Research, 100, 1913-1931.
612 Toramaru, A. (2006). BND (bubble number density) decompression rate meter for explosive
613 volcanic eruptions. Journal of Volcanology and Geothermal Research, 154, 303-316.
614 Webster, J.D., Sintoni, M.F., and De Vivo, B. (2009) The partitioning behavior of Cl, S, and H_2O
615 in aqueous vapor - +/- saline-liquid saturated phonolitic and trachytic melts at 200 MPa.
616 Chemical Geology, 263, 19-36.
617 Zajacz, Z., Candela, P.A., Piccoli, P.M., and Sanchez-Valle, C. (2012) The partitioning of sulfur
618 and chlorine between andesite melts and magmatic volatiles and the exchange coefficients of
619 major cations. Geochimica et Cosmochimica Acta, 89, 81-101.
620 Zhang, Y., and Ni, H. (2010) Diffusion of H, C, and O Components in Silicate Melts. In Y.
621 Zhang and D.J. Cherniak, Eds., Diffusion in Minerals and Melts, 72, p. 171–225. Reviews in
622 Mineralogy, Chantilly, Virginia.

623

624 **LIST OF FIGURE CAPTIONS**

625 **Figure 1.** Microscopic image of sample GYClA-3 (r ~ 0.1 MPa/s; t_A = 5 h). The bubble size
626 ranges from about ~5 to ~80 μm in diameter.

627

628 **Figure 2a-c.** BSE images of products of selected experiments with various decompression rates
629 r. a) QFMClA-1, b) QFMClA-3 and c) QFMClA-5. Values for r are displayed in the upper right
630 corner of each image and t_A = 0 h for the three experiments. Decreasing r leads to a decreasing
631 number of bubbles and an increasing size of bubbles. Some bubbles are elongated and show a
632 preferred orientation (flow structures).

633

634 **Figure 3a-f.** Selected BSE images from experimental series GYMClA. a) and b) GYMClA-1; c)
635 and d) GYMClA-5; e) and f) GYMClA-3. The decompression rate *r* of all three experiments was
636 0.1 MPa/s.

637

638 **Figure 4a-b.** *BND* plotted as a function of decompression rate *r* and annealing time t_A. a)
639 $\log(BND \times mm^3)$ vs. *r* (*logarithmic scaling*). Samples of the experimental series QFMA,
640 QFMClA, GYClA and GYMClA which have been directly quenched after continuous
641 decompression (t_A = 0 h) are plotted together with the results of Cichy et al. (2011; Ci11)
642 obtained for a rhyodacitic melt compositions. Note that decompression experiments of Cichy et
643 al. (2011) with $r \geq 0.1$ MPa/s were conducted applying a continuous decompression technique
644 similar to that in this study, while those with $r \leq 0.01$ MPa/s are carried out using a multi-step
645 approach. b) $\log(BND \times mm^3)$ vs. t_A at constant r = 0.1 MPa/s (experimental series: GYClA and
646 GYMClA).
647 *Horizontal error bars* are smaller than symbol size.
648 *a*: QFMA experiments: ~140 ppm initial S, Cl-free, ~QFM+0.8
649 *b*: QFMClA: ~240 ppm initial S, ~1000 ppm initial Cl, ~QFM+0.8
650 *c*: GYClA: ~1000 ppm initial S, ~1000 ppm initial Cl, ~QFM+1.8
651 *d*: GYMClA: ~1000 ppm initial S, 500 ppm initial Cl, ~QFM+1.8.

652

653 **Figure 5.** Results of this study and previously published data based on continuous decompression
654 experiments and comparison to the trends predicted by the model of Toramaru (2006). The black
655 arrow indicates that two experiments of Mangan and Sisson (2000) conducted at r = 0.025 MPa/s
656 show *BND* of $10^{-0.59}$ mm^{-3} and $10^{-1.32}$ mm^{-3}, respectively.
657 *Horizontal error bars* are smaller than symbol size.

Ci11: Experiments of Cichy et al. (2011); only CO_2-free, continuous decompression experiments are considered; rhyodacite; 850°C

Go11: Gondé et al. (2011); haplogranite; 730 to 1000°C

Ha10: Hamada et al. (2010); rhyolitic obsidian; 700 to 800°C

MS00: Mangan and Sisson (2000); rhyolitic obsidian; 900°C

MBL04: Mourtada-Bonnefoi and Laporte (2004); rhyolite; 800°C

To06: The trends were calculated for rhyolitic and andesitic systems using the model of Toramaru (2006), see text for further details.

homogen.: Homogeneous bubble nucleation

heterogen.: Heterogeneous bubble nucleation

saturated: The melt was H_2O saturated prior to decompression.

a: The andesite-trends were calculated for 1030°C and σ_{LB} = 0.015, 0.028 or 0.063 N/m, assuming average values for the initial the H_2O content in the melt (6.5 wt%) and for ρ_{melt} (2.225 g/cm^3); see text for details.

b: The rhyolite-trend was calculated for 800°C using the values given by Hamada et al. (2010) for C_{SAT}, P_{SAT}, Ω_L and D_{H2O} and assuming a σ_{LB} of 0.08 N/m.

Figure 6a-f. H_2O, S, and Cl contents of the starting glasses and the partially degassed glasses. a) H_2O content vs. *r*; b) H_2O content vs. t_A; c) S content vs. *r*; d) S content vs. t_A; e) Cl content vs. *r*; f) Cl content vs. t_A. The grey shaded area marks the decompression step. The H_2O, S, and Cl contents of all glasses are given in Table 2 of Fiege et al. (2014). The H_2O concentrations within the glasses were measured using IR spectroscopy, while the S and Cl contents were determined using EMP (for details see Fiege et al 2014).

681 **TABLES**

Table 1. Chemical composition (wt%) of the anhydrous Krakatau andesite used as a starting material.

SiO_2	64.79	(59)
TiO_2	1.28	(7)
Al_2O_3	15.62	(22)
FeO_{tot} (a)	4.94	(33)
MnO	0.23	(4)
MgO	1.4	(6)
CaO	4.92	(2)
Na_2O	3.92	(25)
K_2O	1.8	(7)
Total	98.91	(78)

Note: Errors are provided in parentheses: standard deviation (1 sigma) based on EMP analysis; number of EMP analyses: 20.
(a) FeO_{tot}: total Fe concentration in the glass given as FeO

682

683

Table 2. Bubble number densities (*BND*) and surface tension (σ_{LB}).

Sample ID	**log (*BND* × mm^3)** (a)	***r*** **[MPa/s]**	t_A **[h]**	σ_{LB} **[N/m]** (b)	**Sample ID**	**log (*BND* × mm^3)** (a)	***r*** **[MPa/s]**	t_A **[h]**	σ_{LB} **[N/m]** (b)
GYClA; *initial volatile content*: 6.56 (24) wt% H_2O; 1018 (188) ppm S; 1033 (21) ppm Cl					**QFMA**; *initial volatile content*: 6.47 (13) wt% H_2O; 137 (15) ppm S				
GYClA-1	4.92 (28)	0.10	-	0.028 / 0.059	QFMA-1	4.55 (31)	0.10	-	0.029 / 0.060
GYClA-2	4.77 (30)	0.10	1.10	0.029 / 0.060	QFMA-2	4.67 (32)	0.05	-	0.029 / 0.060
GYClA-3	4.00 (60)	0.10	5.00	0.029 / 0.061	QFMA-3	4.37 (11)	0.02	-	0.029 / 0.060
GYClA-4	3.03 (40)	0.10	72.06	0.030 / 0.062	QFMA-4	3.98 (37)	0.01	-	0.029 / 0.061
GYClA-5	4.88 (34)	0.10	1.05	0.029 / 0.060	QFMA-5	2.14 (67)	0.0005	-	0.030 / 0.063
GYMClA; *initial volatile content*: 6.29 (24) wt% H_2O; 1043 (143) ppm S; 510 (10) ppm Cl					**QFMClA**; *initial volatile content*: 6.58 (13) wt% H_2O; 260 (19) ppm S; 1042 (24) ppm Cl				
GYMClA-1	4.68 (64)	0.10	-	0.029 / 0.060	QFMClA-1	4.24 (35)	0.10	-	0.029 / 0.060
GYMClA-3	2.62 (32)	0.10	5.00	0.030 / 0.062	QFMClA-2	4.43 (25)	0.05	-	0.029 / 0.060
GYMClA-4	2.78 (35)	0.10	72.06	0.030 / 0.063	QFMClA-3	3.90 (76)	0.02	-	0.029 / 0.061
GYMClA-5	3.61 (17)	0.10	1.05	0.029 / 0.061	QFMClA-4	3.43 (26)	0.01	-	0.029 / 0.061
					QFMClA-5	2.19 (56)	0.0005	-	0.030 / 0.063

Note: Errors are provided in parentheses: standard deviation (1 sigma) of the six analyses performed (3 BSE images; bubbles at the edges included/exclude; see text for details).
(a): logarithmized *BND* values [mm^{-3}].
(b): calculateted for ΔP = 20 MPa (first value) or 60 MPa (second value); see text for details.
- : t_A = 0 h; relative error of *r*: ~7 % ; error of σ_{LB}: ±0.003 N/m

684

685

FIGURES

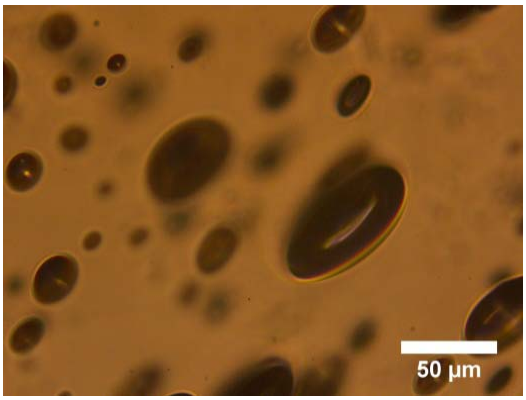

Figure 1. Microscopic image of sample GYClA-3 (r ~ 0.1 MPa/s; t_A = 5 h). The bubble size ranges from about ~5 to ~80 µm in diameter.

686

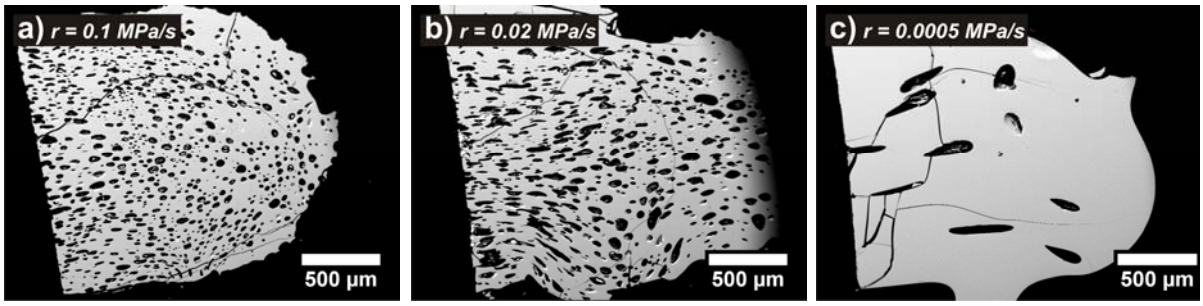

Figure 2a-c. BSE images of products of selected experiments with various decompression rates r. a) QFMClA-1, b) QFMClA-3 and c) QFMClA-5. Values for r are displayed in the upper right corner of each image and t_A = 0 h for the three experiments. Decreasing r leads to a decreasing number of bubbles and an increasing size of bubbles. Some bubbles are elongated and show a preferred orientation (flow structures).

687

688

689

690

691

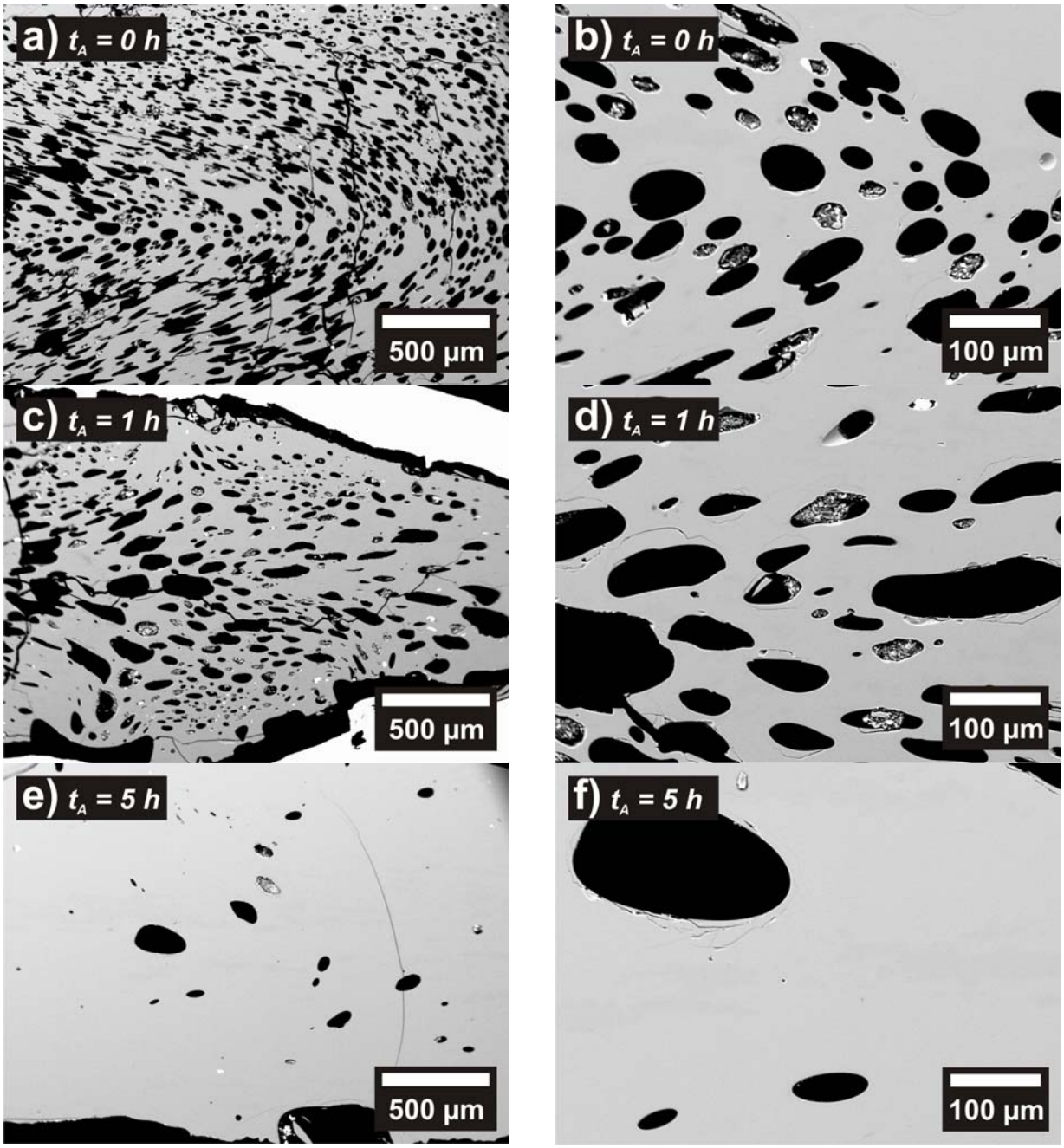

Figure 3a-f. Selected BSE images from experimental series GYMClA. a) and b) GYMClA-1; c) and d) GYMClA-5; e) and f) GYMClA-3. The decompression rate *r* of all three experiments was 0.1 MPa/s.

692

693

694

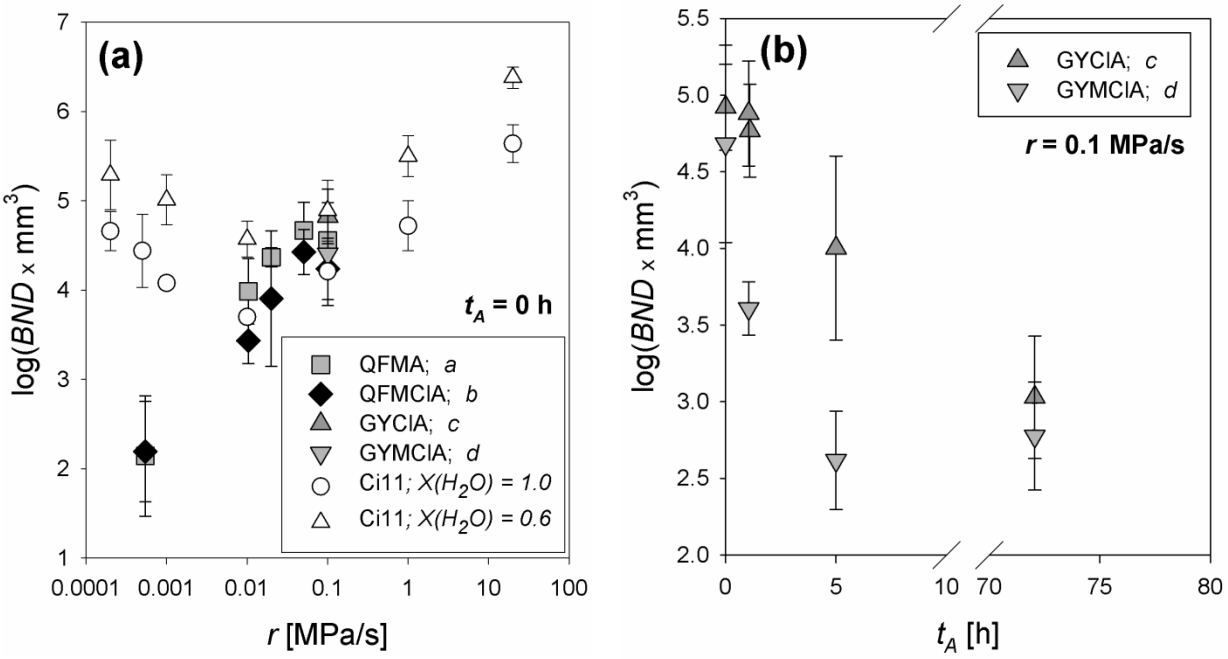

Figure 4a-b. *BND* plotted as a function of decompression rate *r* and annealing time t_A. a) log(*BND* × mm^3) vs. *r* (*logarithmic scaling*). Samples of the experimental series QFMA, QFMClA, GYClA and GYMClA which have been directly quenched after continuous decompression (t_A = 0 h) are plotted together with the results of Cichy et al. (2011; Ci11) on rhyodacitic melt compositions. Here, decompression experiments of Cichy et al. (2011) with $r \geq 0.1$ MPa/s were conducted applying the same continuous decompression technique, while those with $r \leq 0.01$ MPa/s are carried out using a multi-step approach. b) log(*BND* × mm^3) vs. t_A at constant r = 0.1 MPa/s (experimental series: GYClA and GYMClA).
Horizontal error bars are smaller than symbol size.
a: QFMA experiments: ~140 ppm initial S, Cl-free, ~QFM+0.8
b: QFMClA: ~240 ppm initial S, ~1000 ppm initial Cl, ~QFM+0.8
c: GYClA: ~1000 ppm initial S, ~1000 ppm initial Cl, ~QFM+1.8
d: GYMClA: ~1000 ppm initial S, 500 ppm initial Cl, ~QFM+1.8.

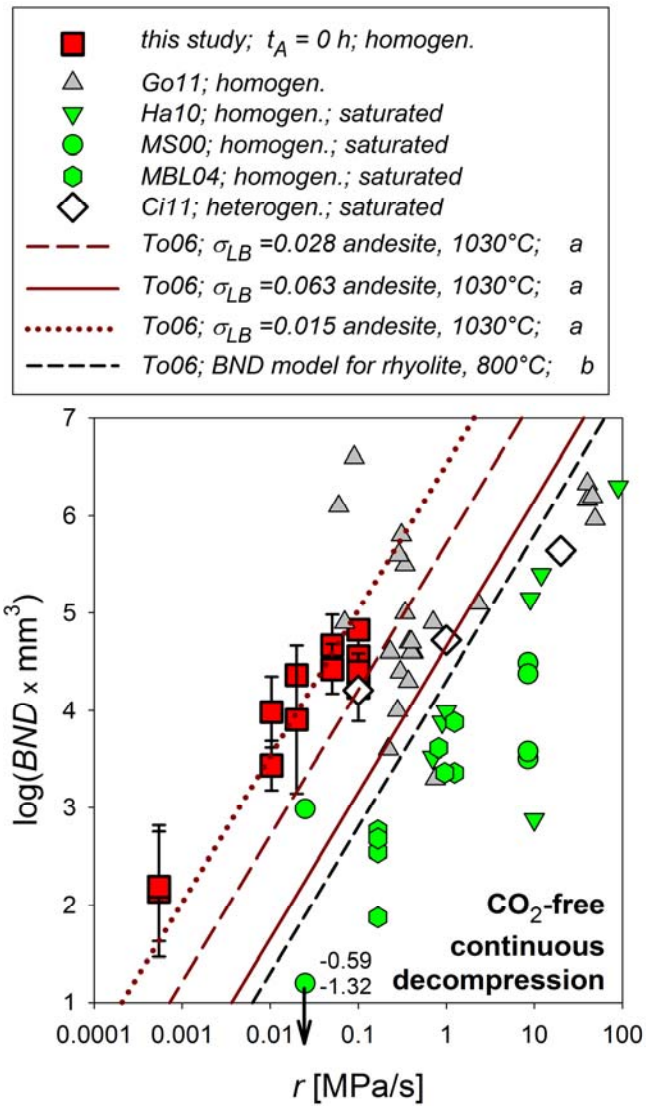

Figure 5. Results of this study and previously published data based on continuous decompression experiments and comparison to the trends predicted by the model of Toramaru (2006). The black arrow indicates that two experiments of Mangan and Sisson (2000) conducted at r = 0.025 MPa/s show *BND* of $10^{-0.59}$ mm^{-3} and $10^{-1.32}$ mm^{-3}, respectively.

Horizontal error bars are smaller than symbol size.

Ci11: Experiments of Cichy et al. (2011); only CO_2-free, continuous decompression experiments are considered; rhyodacite; 850°C

Go11: Gondé et al. (2011); haplogranite; 730 to 1000°C

Ha10: Hamada et al. (2010); rhyolitic obsidian; 700 to 800°C

MS00: Mangan and Sisson (2000); rhyolitic obsidian; 900°C

MBL04: Mourtada-Bonnefoi and Laporte (2004); rhyolite; 800°C

To06: The trends were calculated for rhyolitic and andesitic systems using the model of Toramaru (2006), see text for further details.

homogen.: Homogeneous bubble nucleation

heterogen.: Heterogeneous bubble nucleation

saturated: The melt was H_2O saturated prior to decompression.

a: The andesite-trends were calculated for 1030°C and σ_{LB} = 0.015, 0.028 or 0.063 N/m, assuming average values for the initial H_2O content in the melt (6.5 wt%) and for ρ_{melt} (2.225 g/cm^3); see text for details.

b: The rhyolite-trend was calculated for 800°C using the values given by Hamada et al. (2010) for C_{SAT}, P_{SAT}, Ω_L and D_{H2O} and assuming a σ_{LB} of 0.08 N/m.

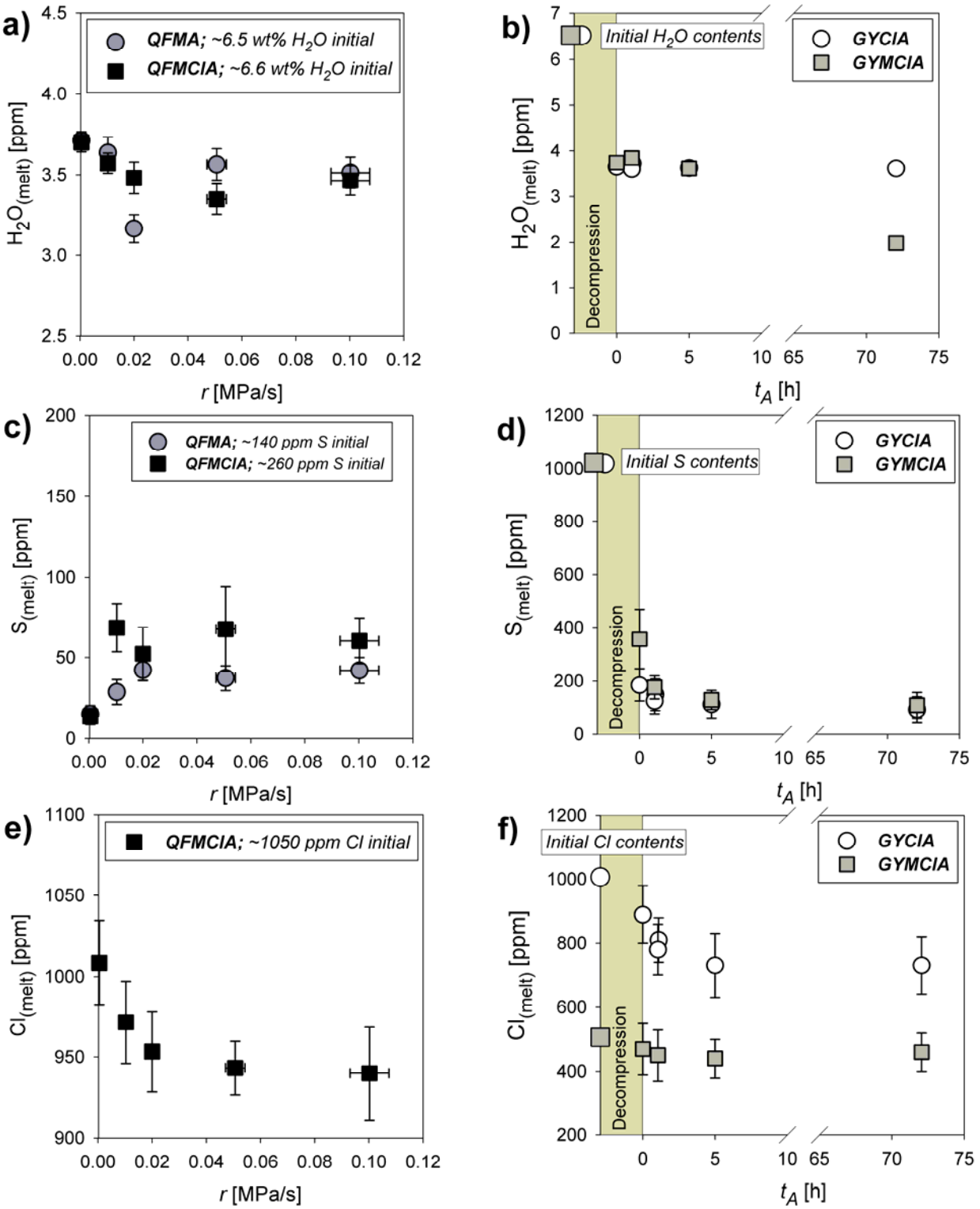

Figure 6a-f. H_2O, S, and Cl contents of the starting glasses and the partially degassed glasses. a) H_2O content vs. r; b) H_2O content vs. t_A; c) S content vs. r; d) S content vs. t_A; e) Cl content vs. r; f) Cl content vs. t_A. The grey shaded area marks the decompression step. The H_2O, S, and Cl contents of all glasses are given in Table 2 of Fiege et al. (2014). The H_2O concentrations within the glasses were measured using IR spectroscopy, while the S and Cl contents were determined using EMP (for details see Fiege et al 2014).

695

50 µm

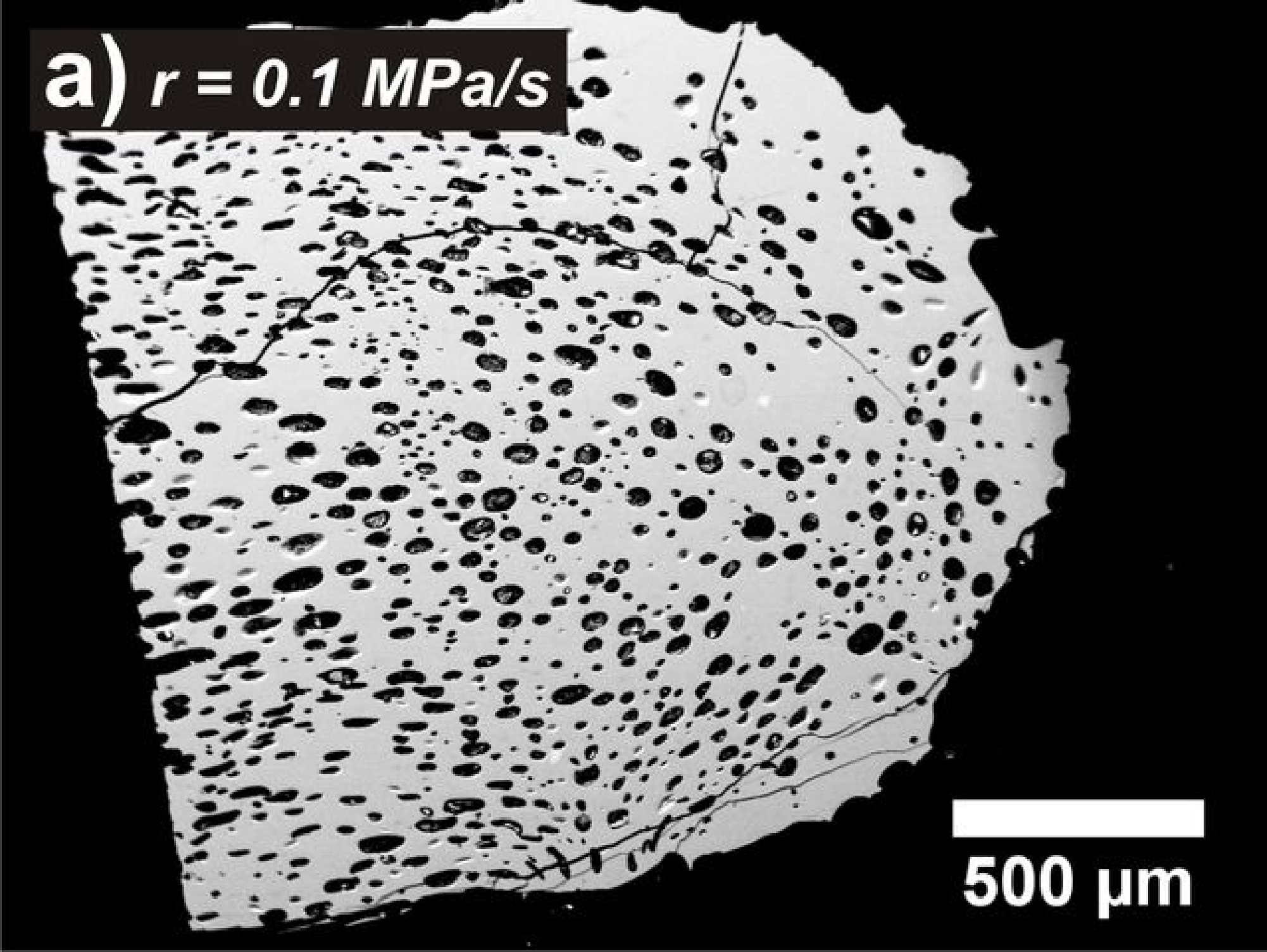
a) r = 0.1 MPa/s
500 µm

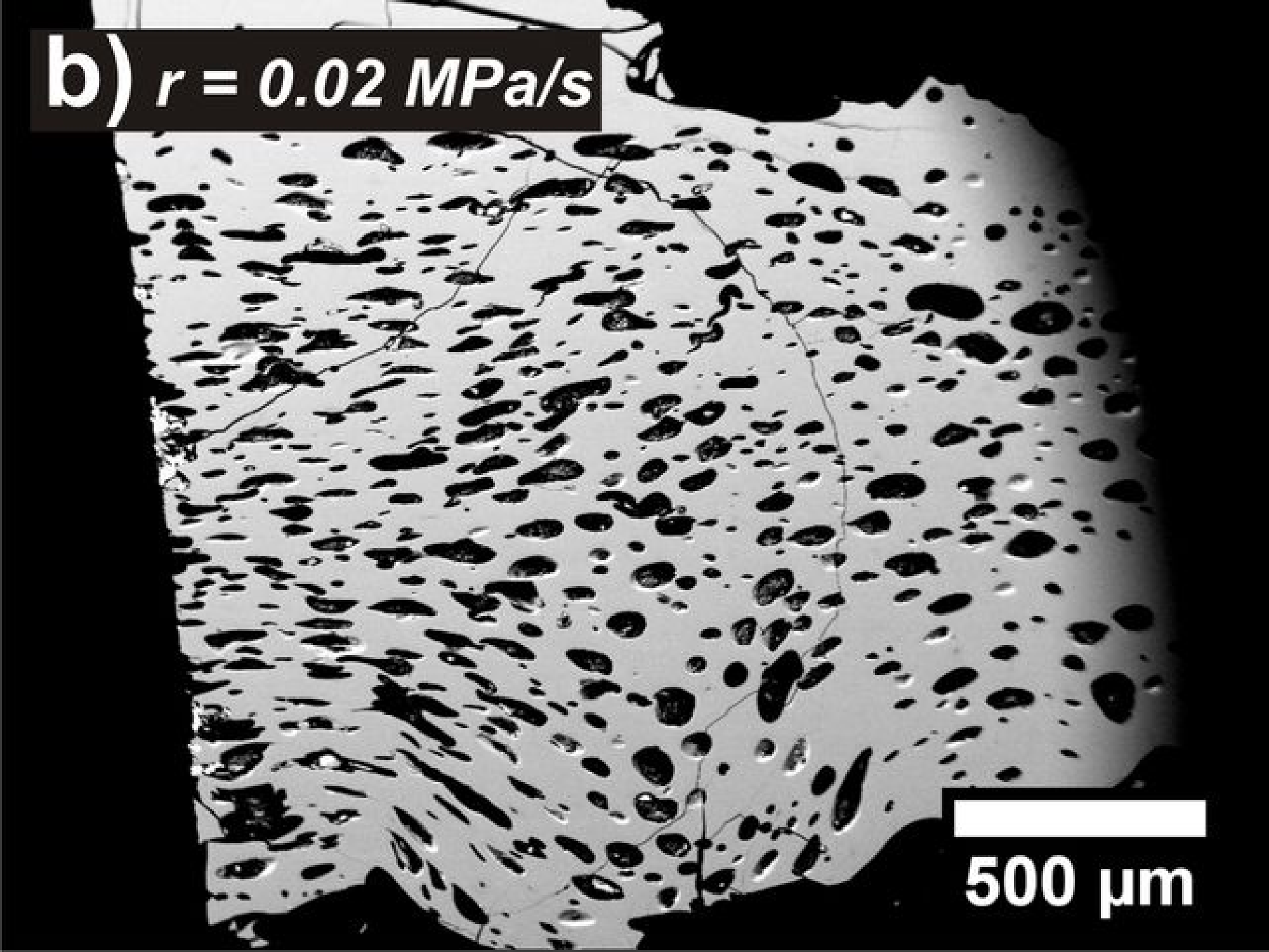
b) r = 0.02 MPa/s
500 µm

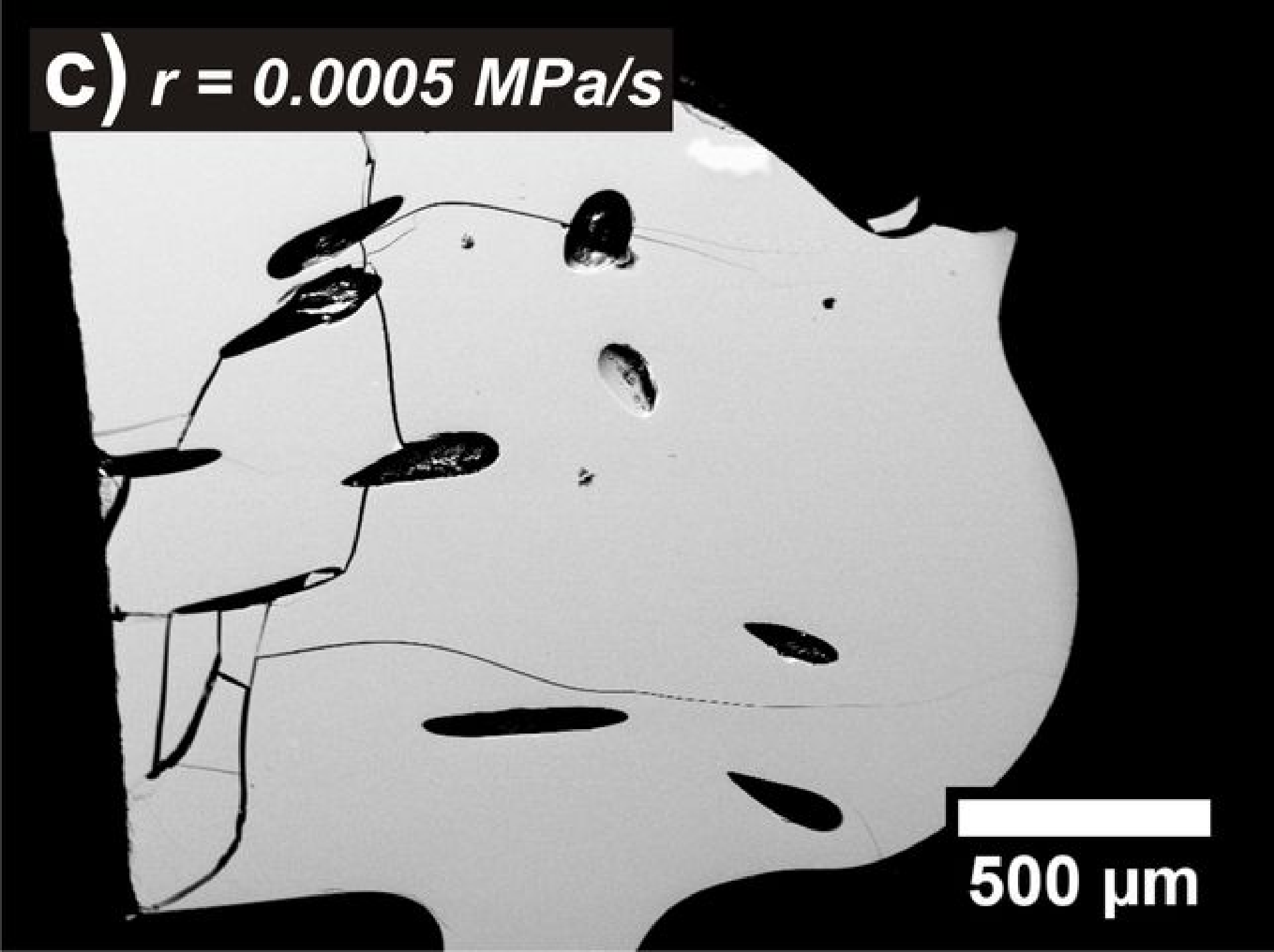
C) r = 0.0005 MPa/s
500 µm

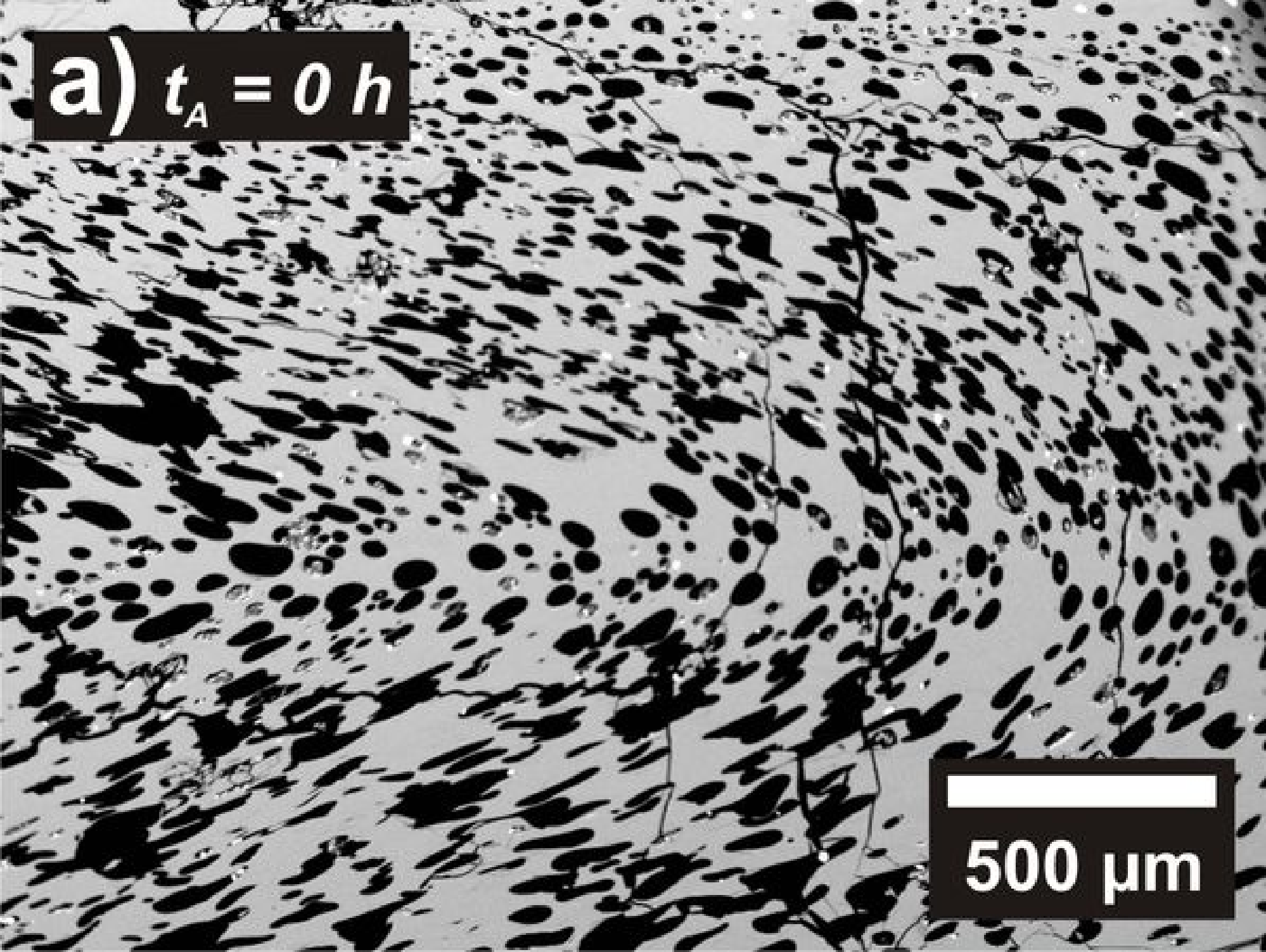
a) t_A = 0 h
500 µm

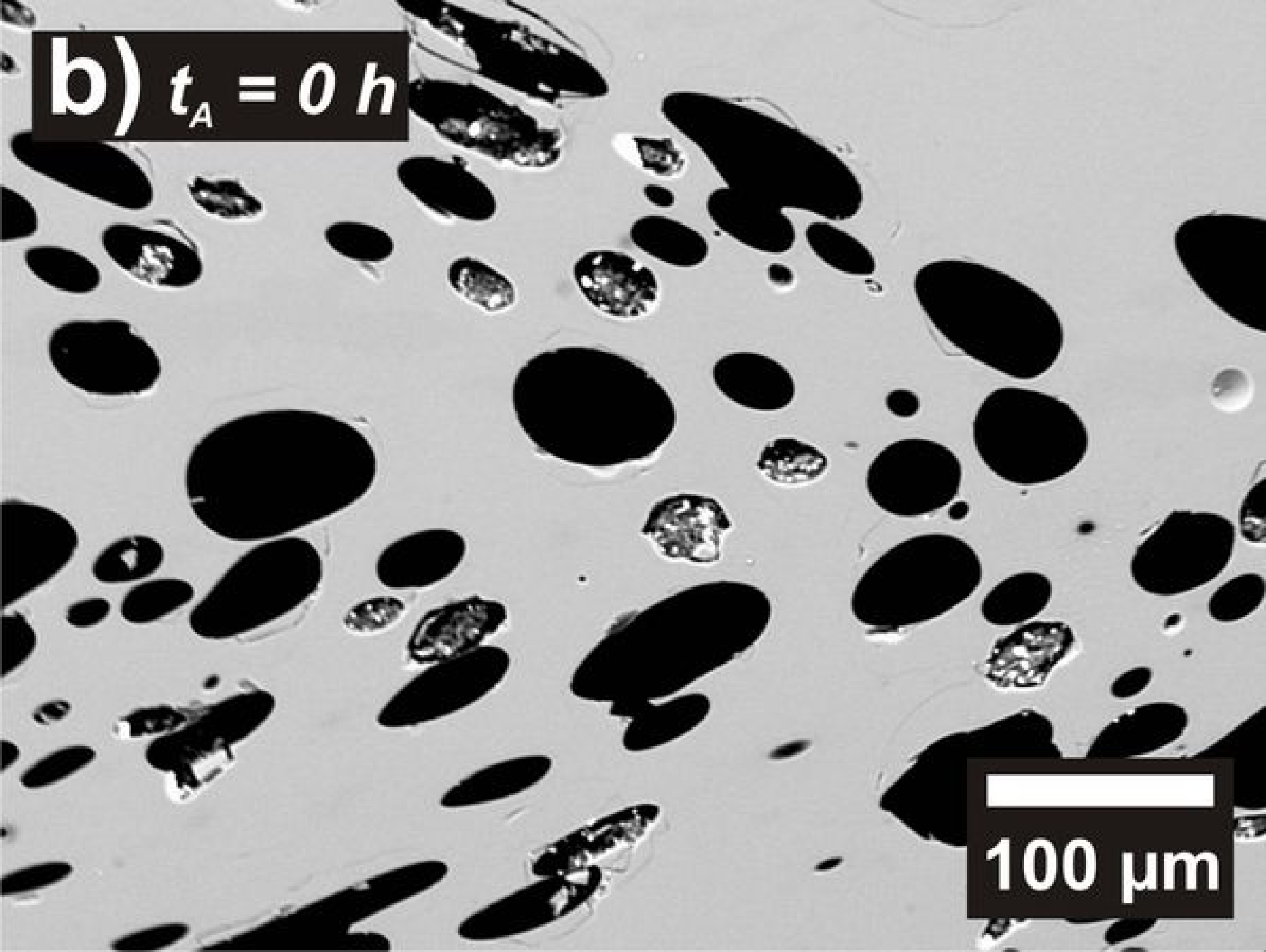
b) t_A = 0 h
100 µm

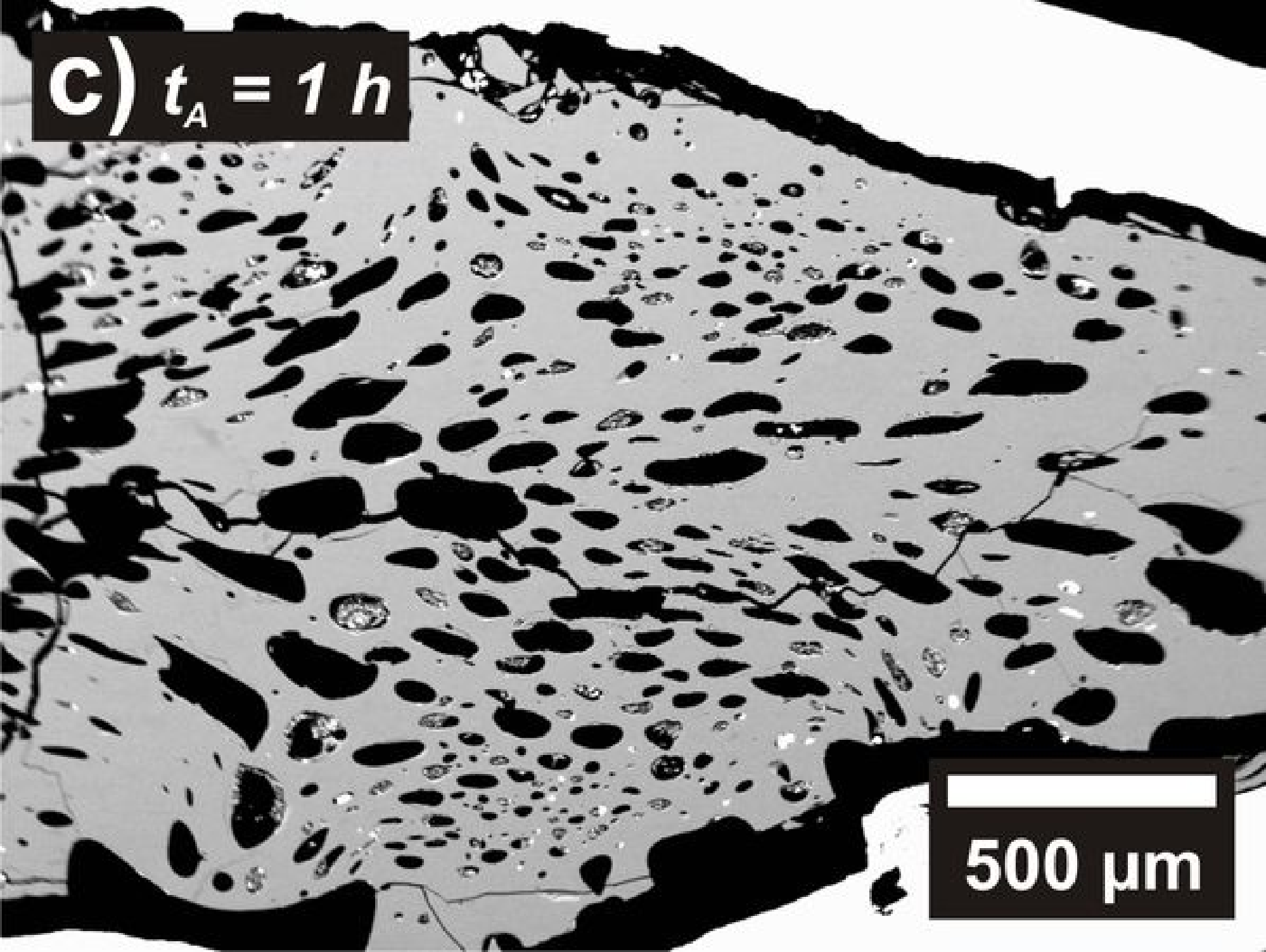
c) t_A = 1 h
500 µm

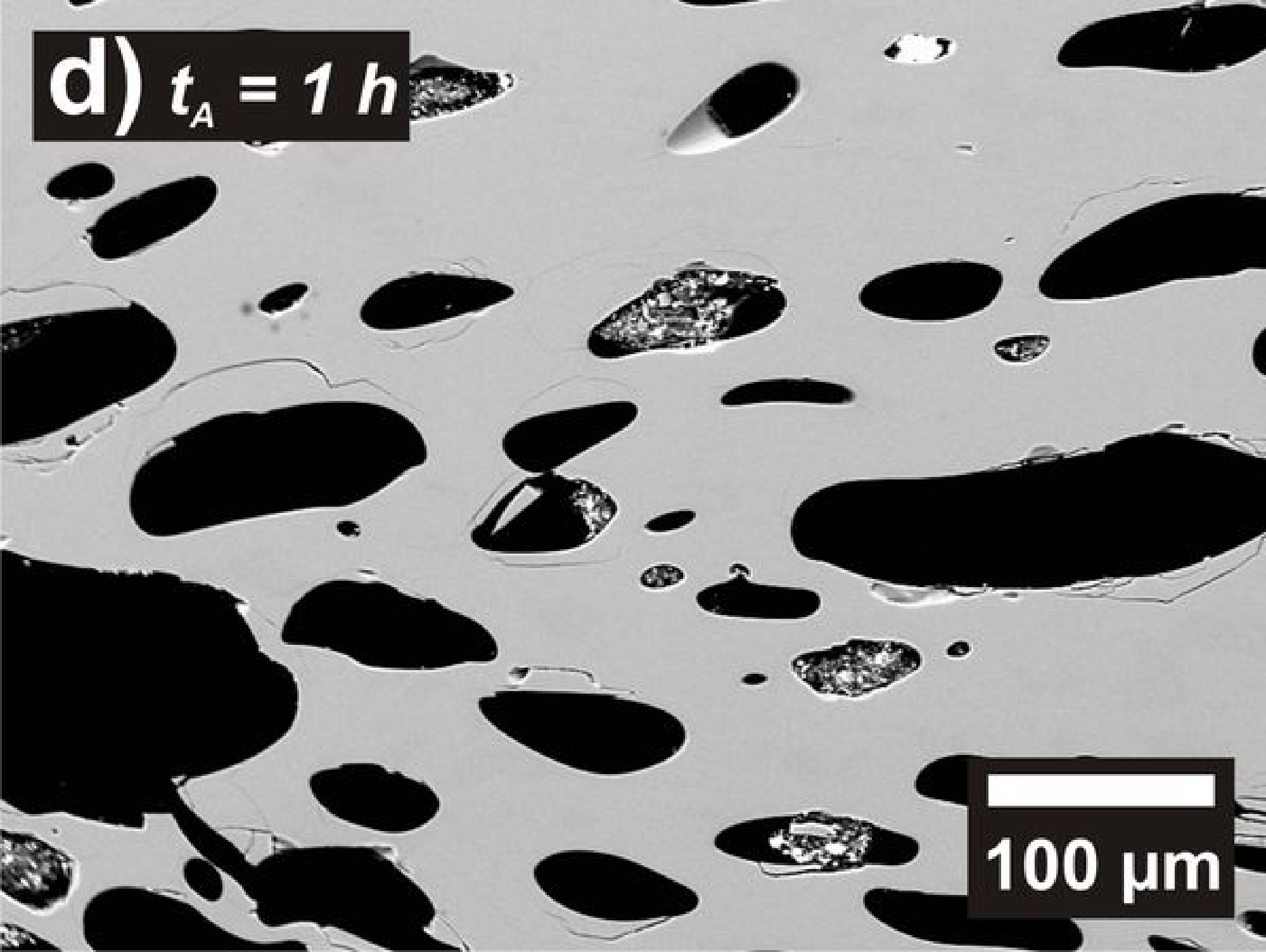
d) t_A = 1 h
100 µm

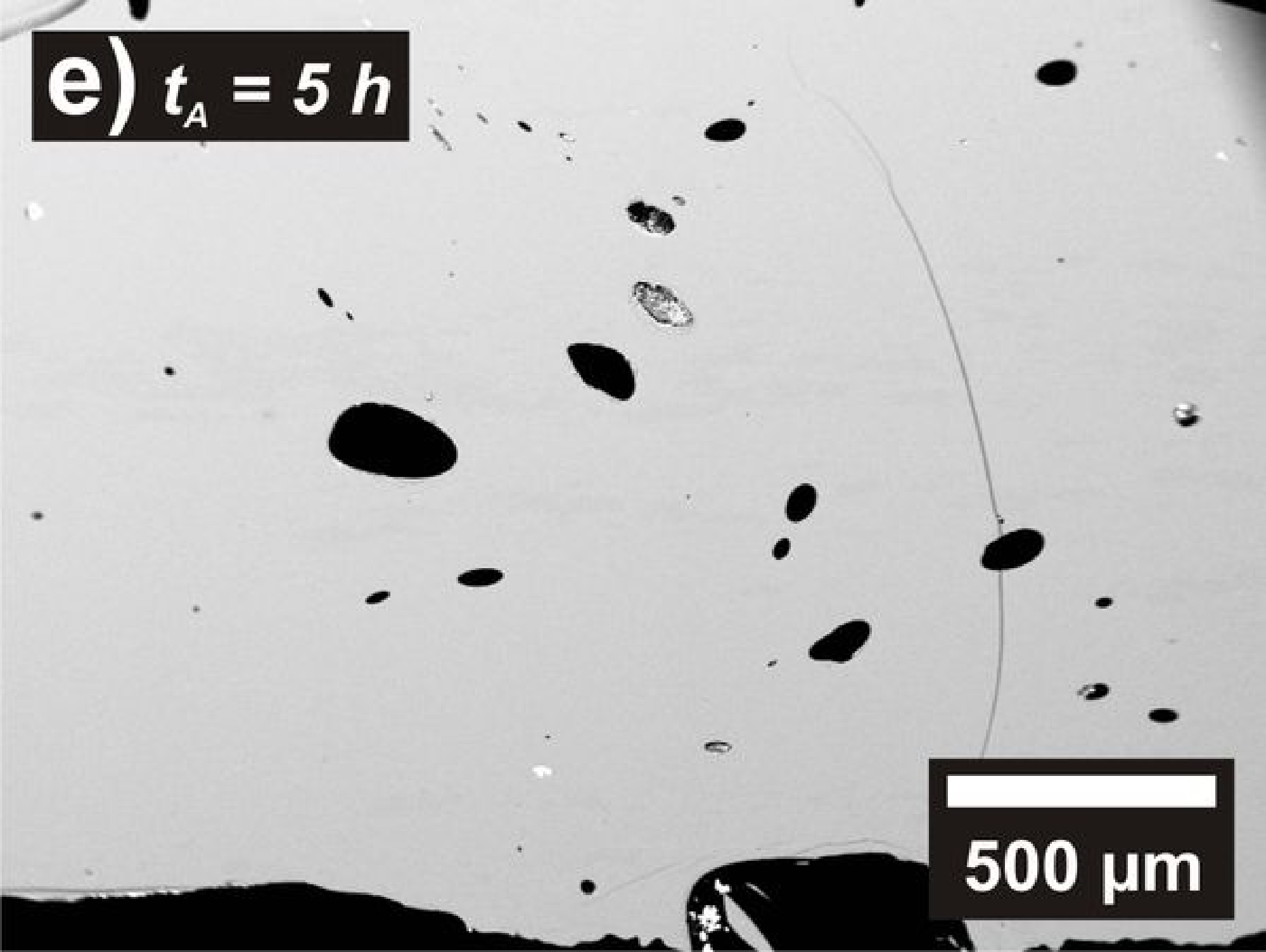
e) t_A = 5 h
500 µm

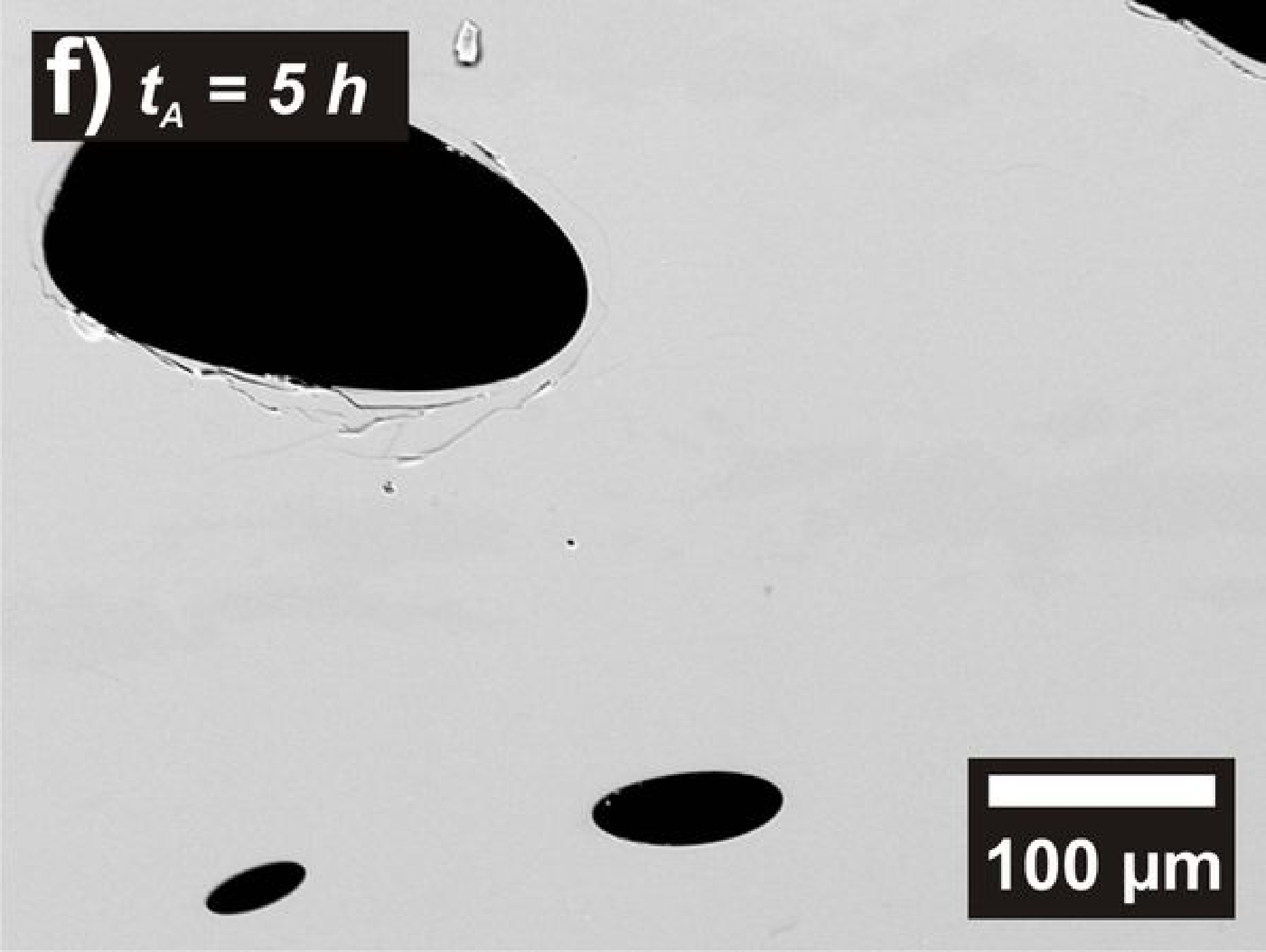
f) t_A = 5 h
100 µm

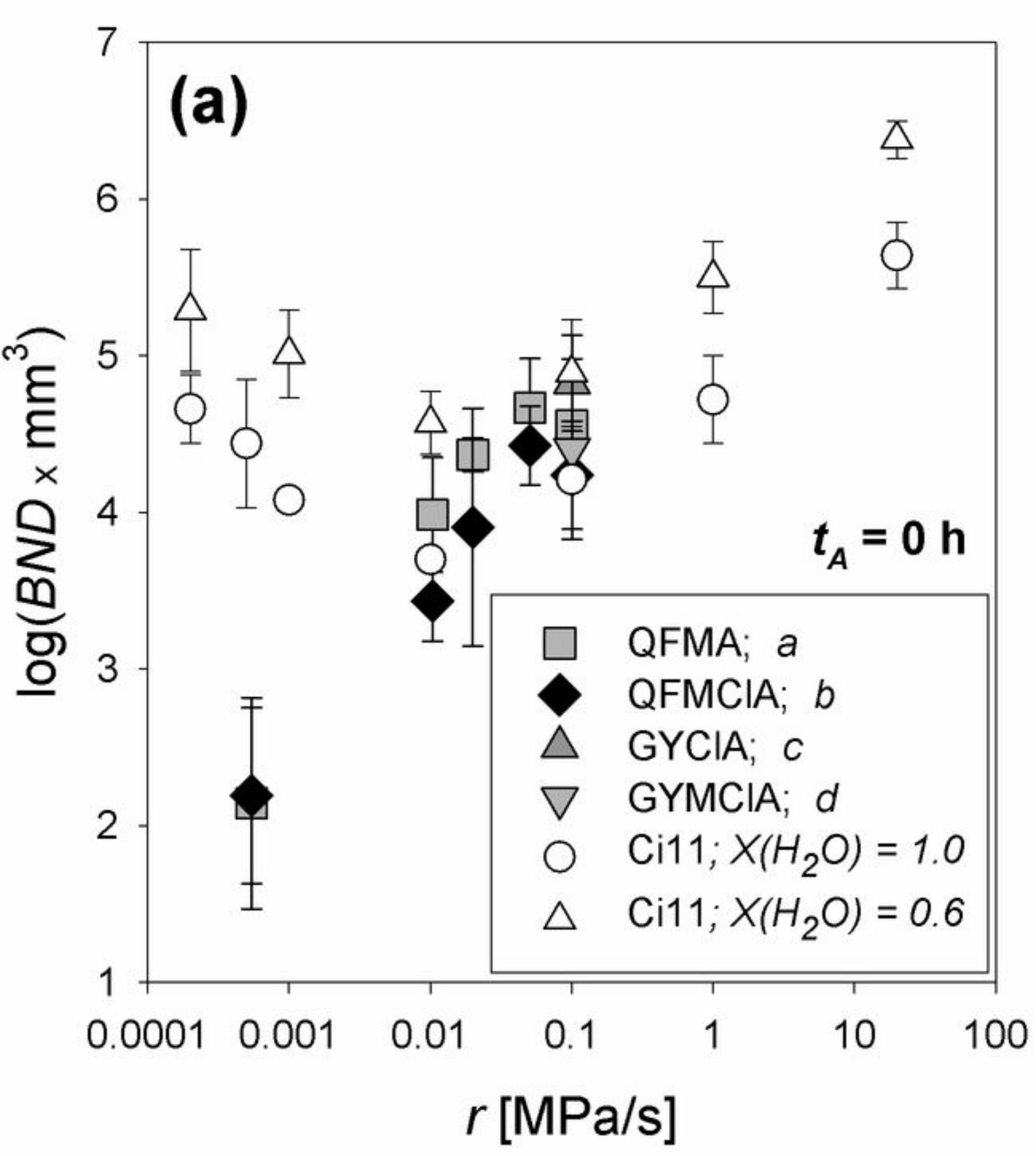
(a)
7
6
5
4
3
2
1
log(BND x mm3)
0.0001
0.001
0.01
0.1
1
10
100
r [MPa/s]
tA = 0 h
QFMA; a
QFMCIA; b
GYCIA; c
GYMCIA; d
Ci11; X(H2O) = 1.0
Ci11; X(H2O) = 0.6

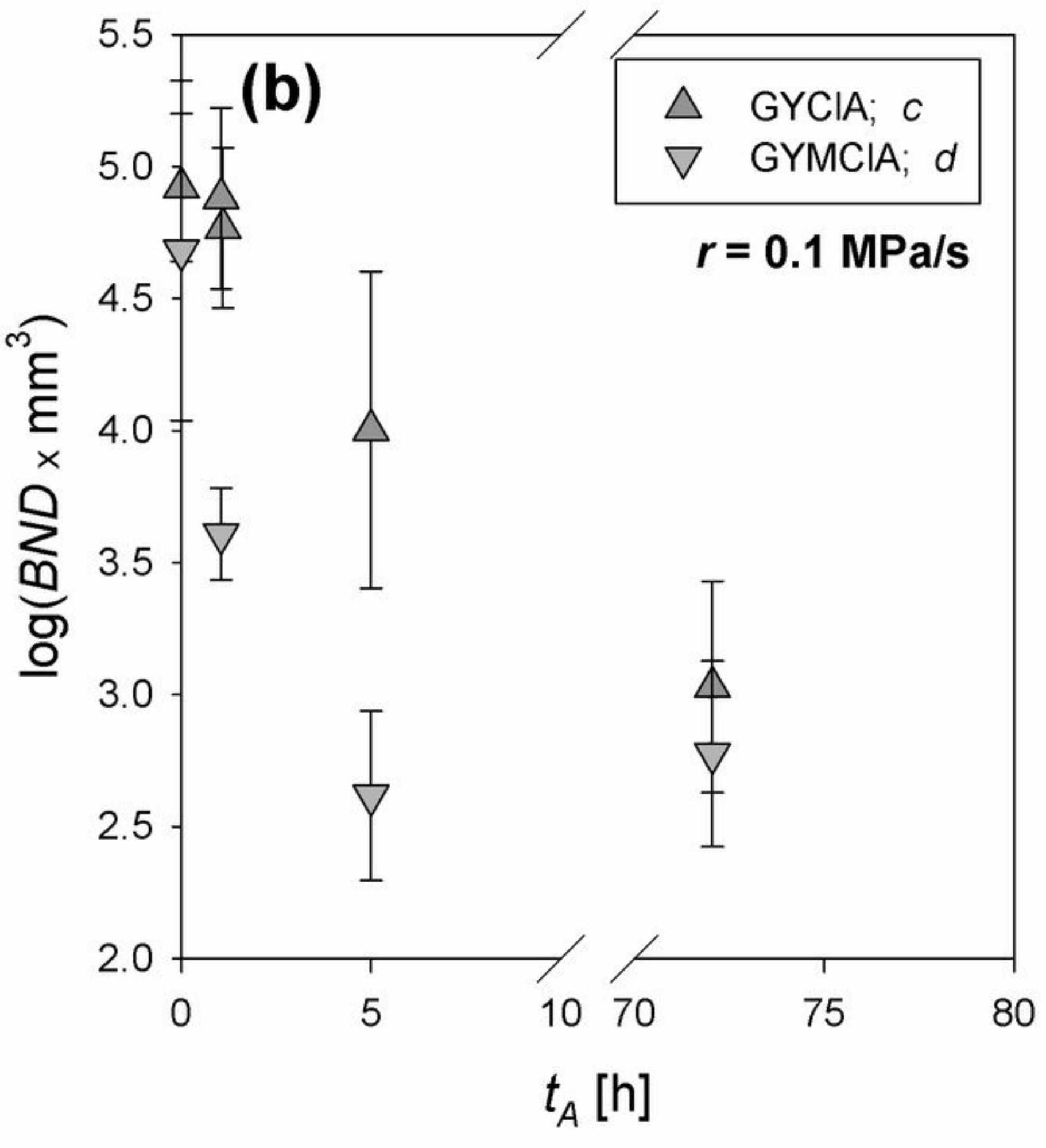
(b)
GYCIA; c
GYMCIA; d
r = 0.1 MPa/s
log(BND x mm3)
5.5
5.0
4.5
4.0
3.5
3.0
2.5
2.0
0
5
10
70
75
80
tA [h]

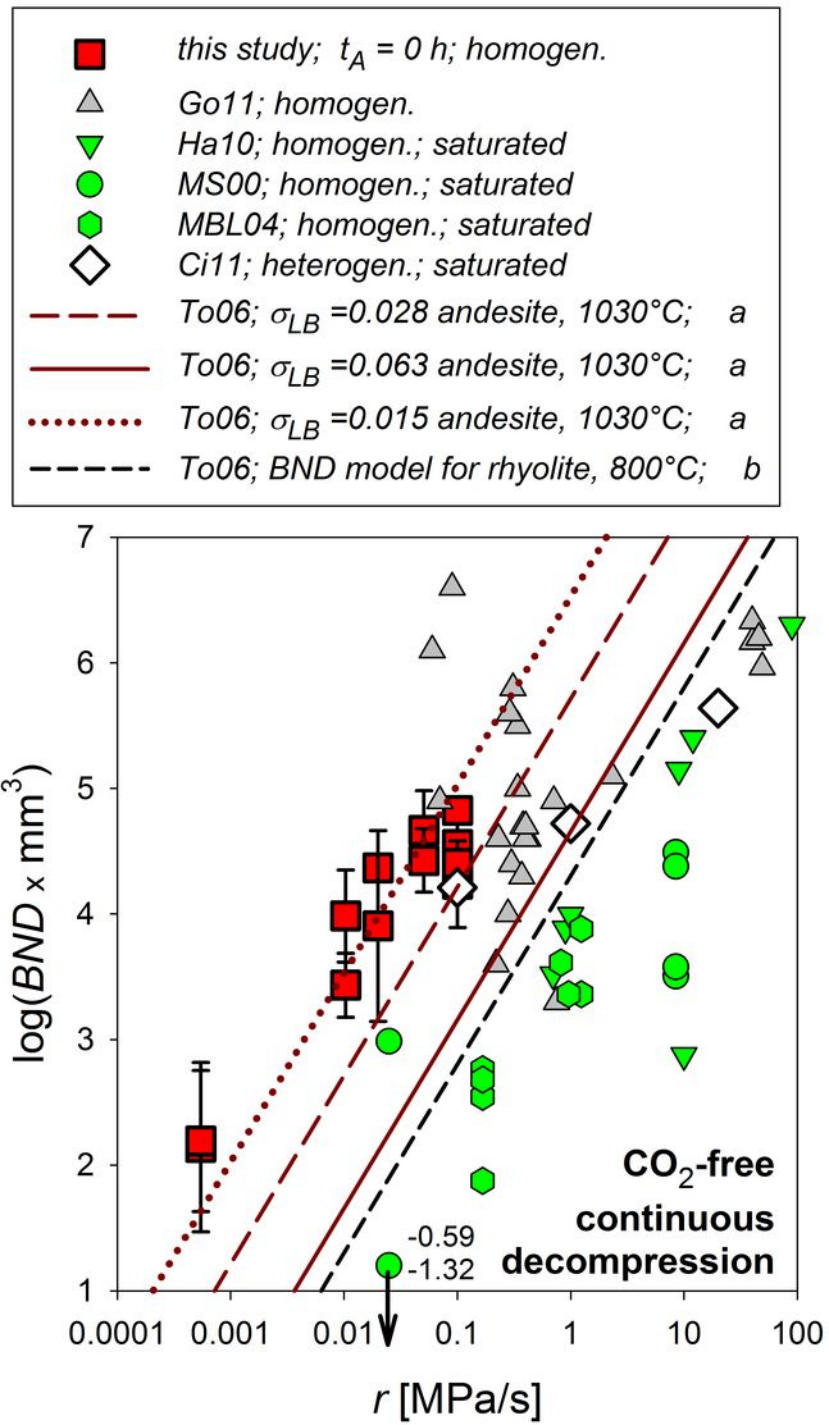
this study; t_A = 0 h; homogen.
Go11; homogen.
Ha10; homogen.; saturated
MS00; homogen.; saturated
MBL04; homogen.; saturated
Ci11; heterogen.; saturated
To06; σ_{LB} =0.028 andesite, 1030°C; a
To06; σ_{LB} =0.063 andesite, 1030°C; a
To06; σ_{LB} =0.015 andesite, 1030°C; a
To06; BND model for rhyolite, 800°C; b
log(BND x mm^3)
7
6
5
4
3
2
1
CO$_2$-free
continuous
decompression
-0.59
-1.32
0.0001
0.001
0.01
0.1
1
10
100
r [MPa/s]

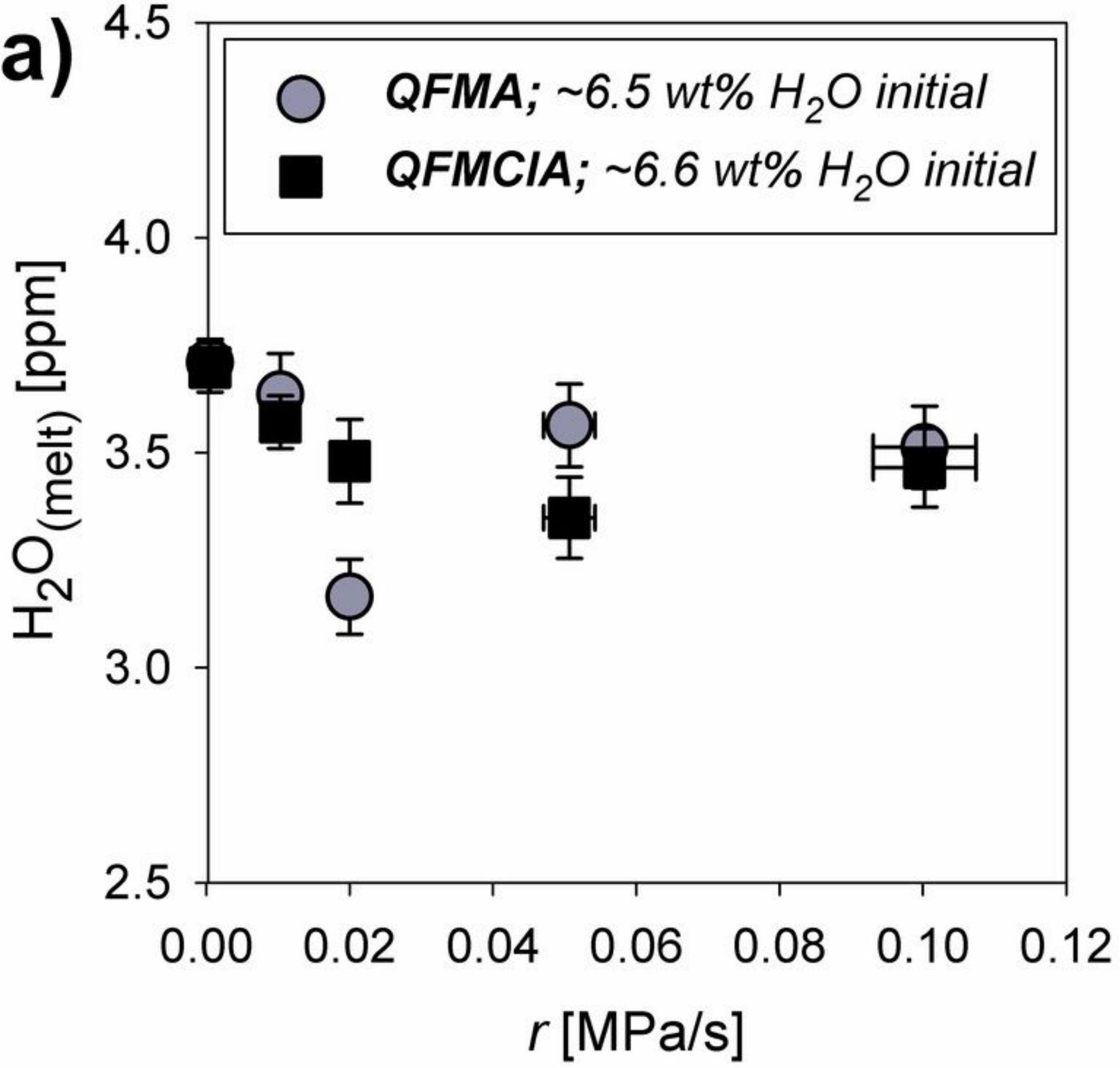
a)
QFMA; ~6.5 wt% H2O initial
QFMCIA; ~6.6 wt% H2O initial
H2O(melt) [ppm]
4.5
4.0
3.5
3.0
2.5
0.00
0.02
0.04
0.06
0.08
0.10
0.12
r [MPa/s]

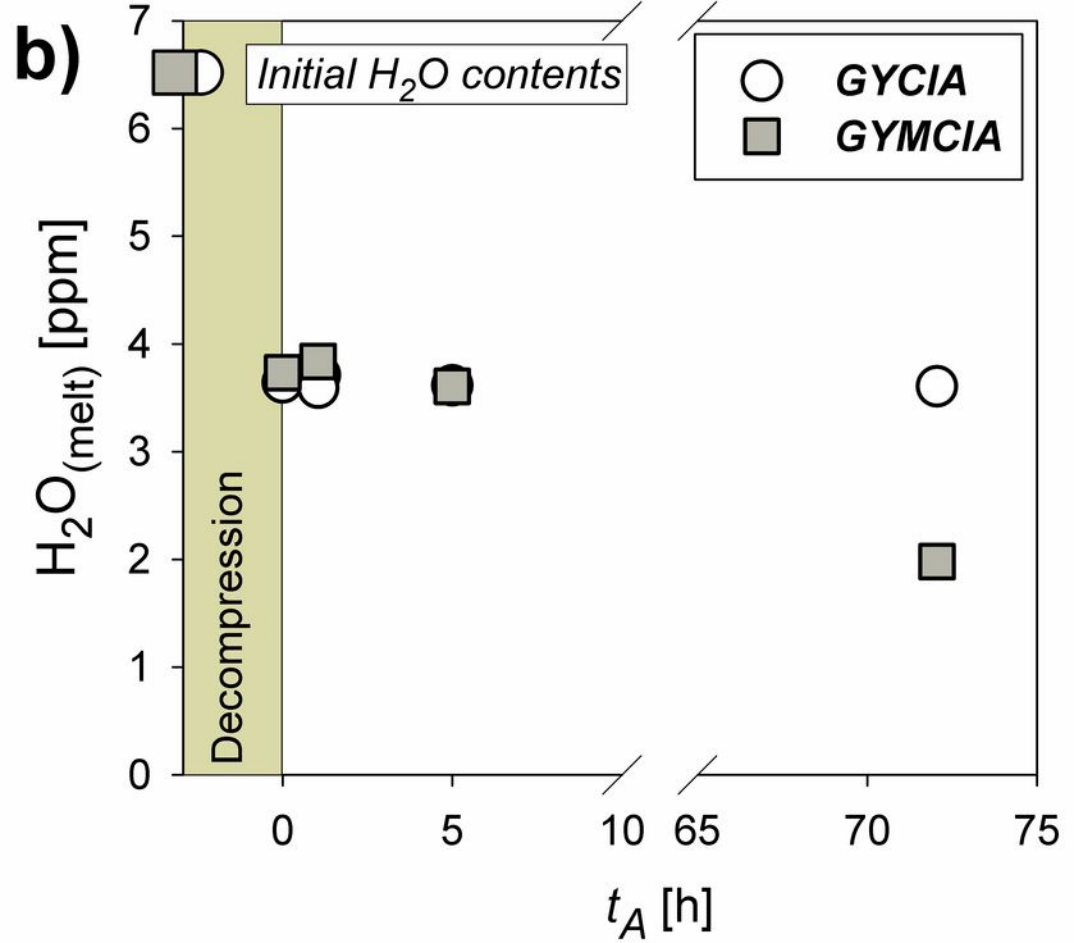
b)
Initial H_2O contents
GYCIA
GYMCIA
$H_2O_{(melt)}$ [ppm]
Decompression
0
1
2
3
4
5
6
7
0
5
10
65
70
75
t_A [h]

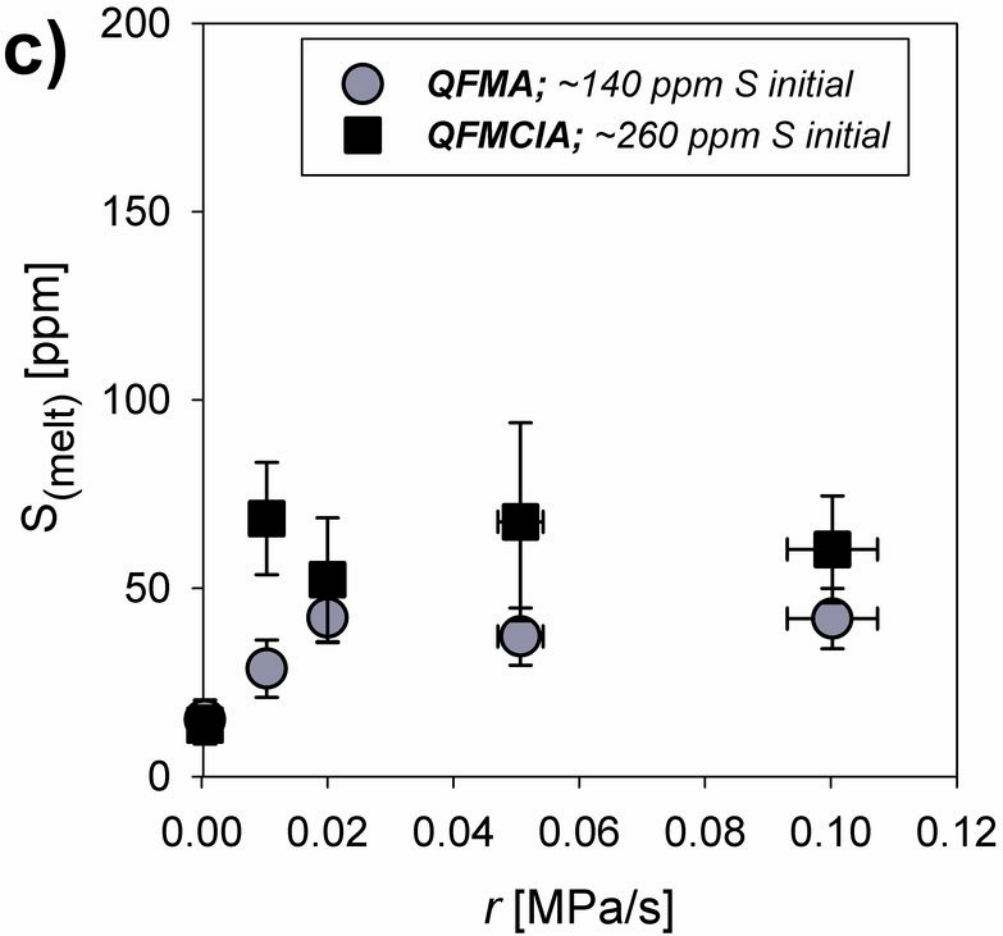
c)
QFMA; ~140 ppm S initial
QFMCIA; ~260 ppm S initial
S(melt) [ppm]
0
50
100
150
200
0.00
0.02
0.04
0.06
0.08
0.10
0.12
r [MPa/s]

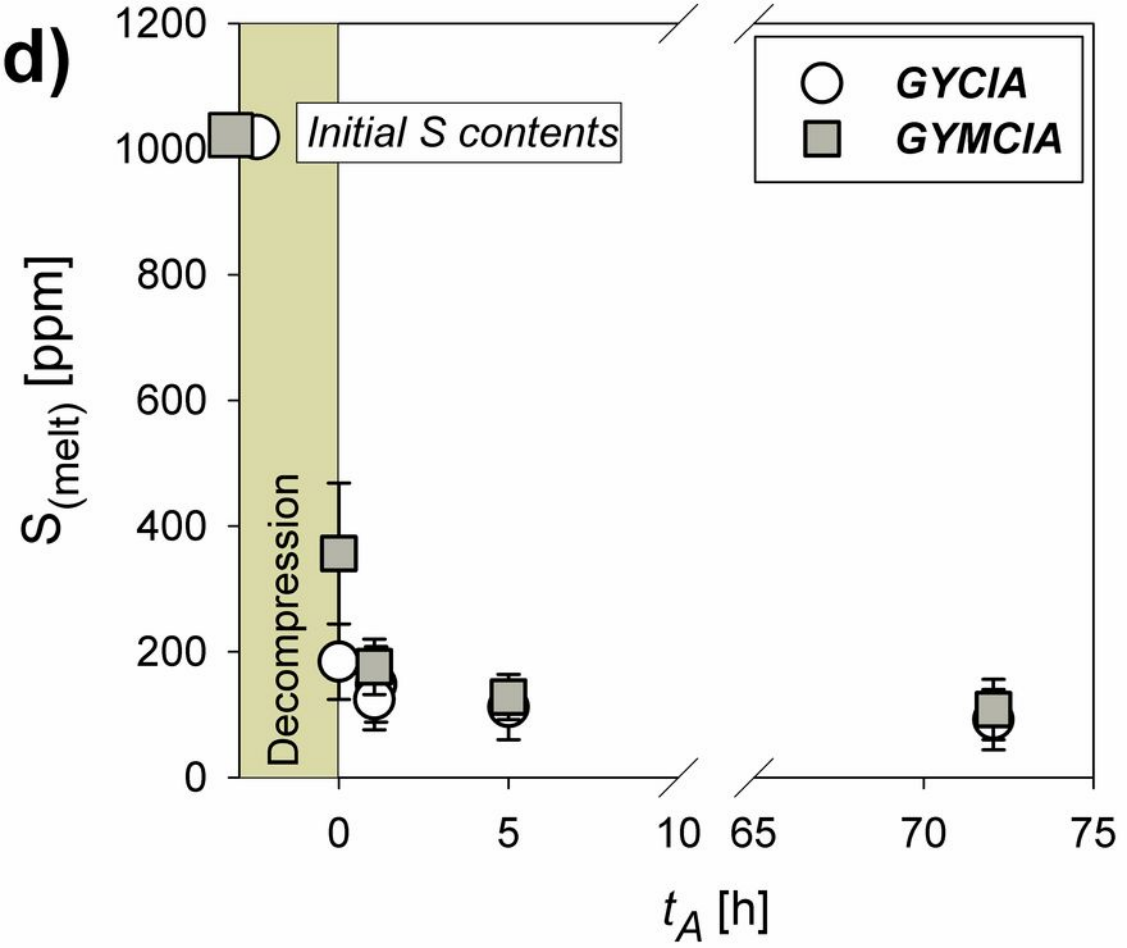
d)
1200
1000
800
600
400
200
0
$S_{(melt)}$ [ppm]
Initial S contents
Decompression
GYCIA
GYMCIA
0
5
10
65
70
75
t_A [h]

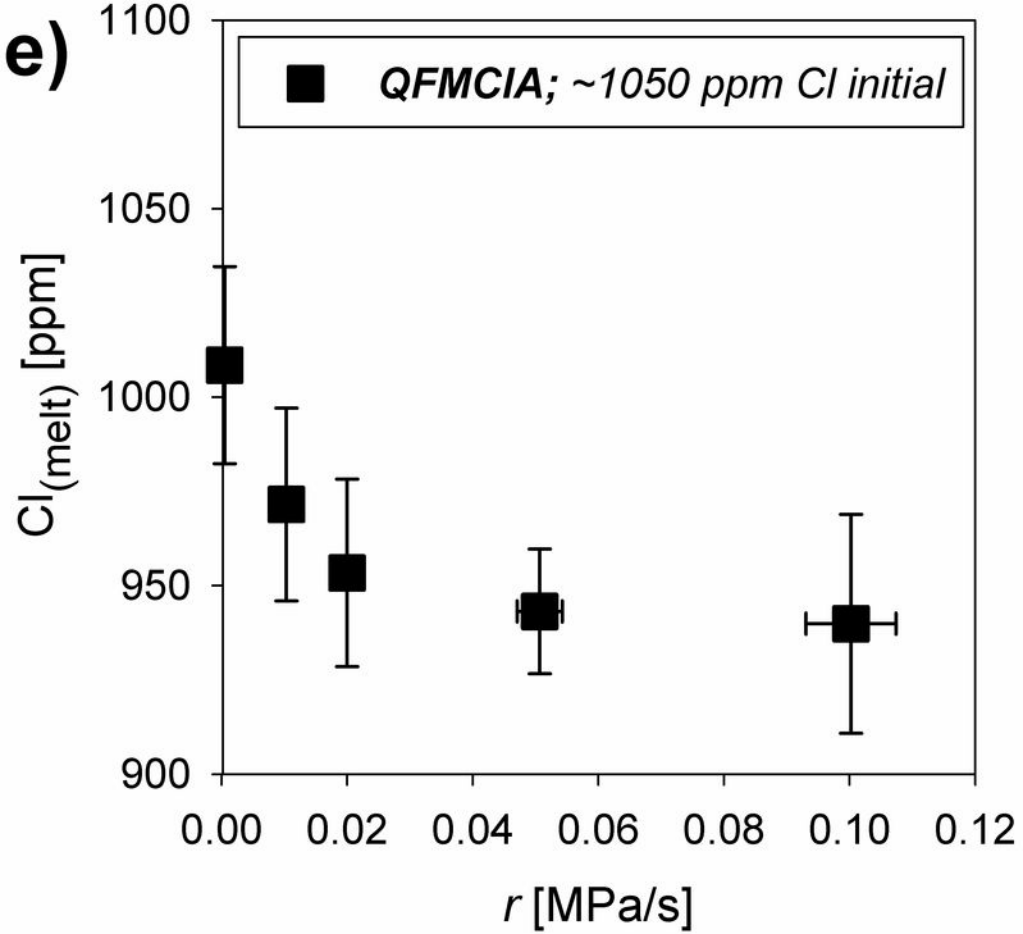
e)
QFMCIA; ~1050 ppm Cl initial
1100
1050
1000
950
900
Cl(melt) [ppm]
0.00
0.02
0.04
0.06
0.08
0.10
0.12
r [MPa/s]

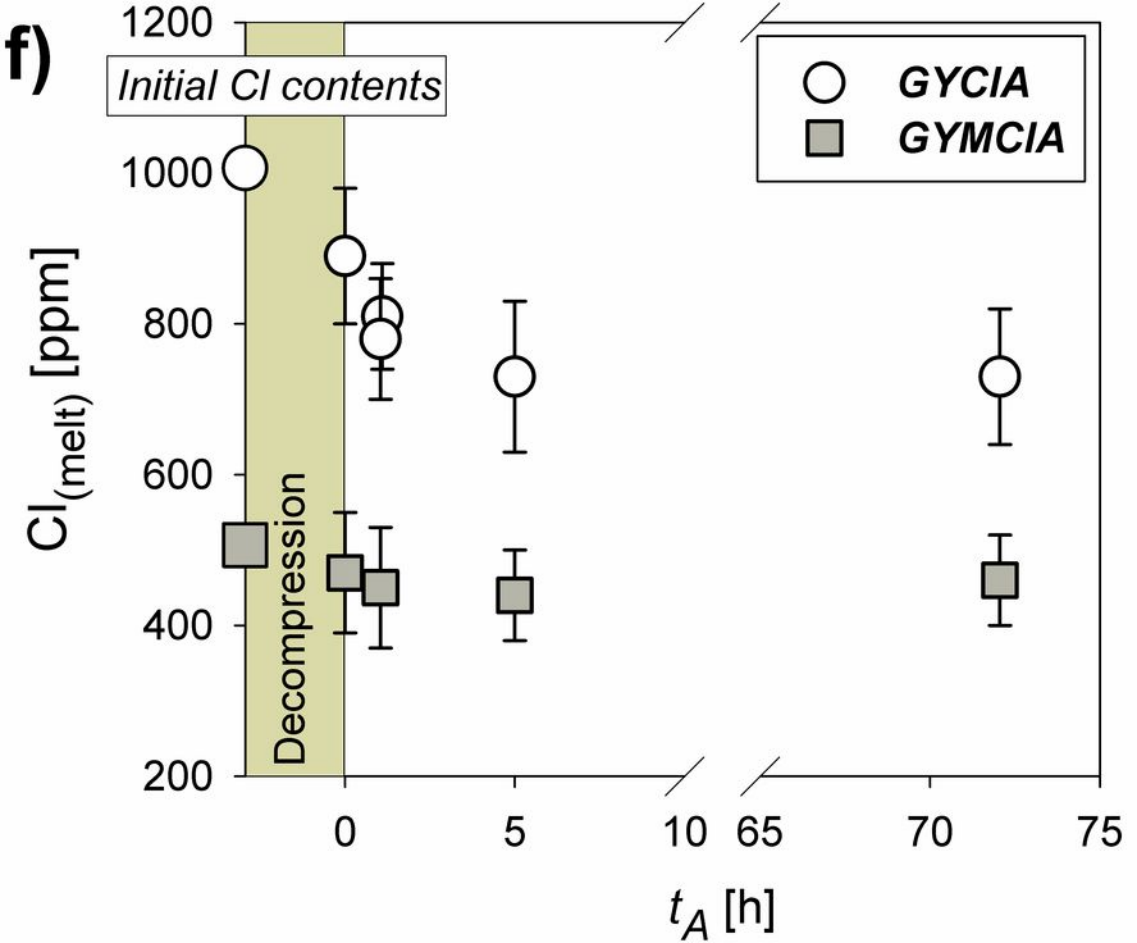
f)
Initial Cl contents
GYCIA
GYMCIA
Decompression
$Cl_{(melt)}$ [ppm]
1200
1000
800
600
400
200
0
5
10
65
70
75
t_A [h]